JPL PUBLICATION 85-39



# NASA/JPL Aircraft SAR Workshop Proceedings

## February 4-5, 1985, at the Jet Propulsion Laboratory, Pasadena, California

N. Donovan
D. Evans
D. Held
Editors



June 15, 1985

National Aeronautics and
Space Administration

**Jet Propulsion Laboratory**
California Institute of Technology
Pasadena, California

JPL PUBLICATION 85-39

# NASA/JPL Aircraft SAR Workshop Proceedings

## February 4-5, 1985, at the Jet Propulsion Laboratory, Pasadena, California

N. Donovan
D. Evans
D. Held
Editors

June 15, 1985

National Aeronautics and
Space Administration

**Jet Propulsion Laboratory**
California Institute of Technology
Pasadena, California

This publication was prepared by the Jet Propulsion Laboratory, California Institute of Technology, under a contract with the National Aeronautics and Space Administration.

ACKNOWLEDGMENT

This workshop was arranged as a forum for the exchange of intermediate results and investigational approaches. Many of the speakers provided papers that grew as this publication was compiled. Unfortunately, these had to be truncated to maintain a summary format and to reflect the spirit of the workshop.

We wish to thank all of the speakers for their cooperation in providing summaries, figures, and images, and, most importantly, for sharing their work with those of us who were fortunate enough to hear the presentations. Thanks also to the attendees who played vital roles in questioning, supporting, and suggesting alternatives during the meetings, as well as augmenting the less formal discussions surrounding this workshop.

We would also like to thank the JPL personnel involved in producing the SAR image data, without which there would have been nothing to talk about. They are:

T. Andersen
R. Blakely
W. E. Brown, Jr.
G. Digiorgi
N. Donovan
W. Fiechter
J. Gilstrap
J. Granger
D. Harrison
A. Holmes
T. Joo
J. McCluskey
E. McMillan
T. Miller
G. Nelson
L. Olivieri
M. Paller
T. Sato
W. Skotnicki
T. W. Thompson
B. Trinh
C. Werner
G. Williams
H. Zebker

## ABSTRACT

Speaker-supplied summaries of the talks given at the NASA/JPL Aircraft SAR Workshop on February 4 and 5, 1985, are provided. These talks dealt mostly with composite quadpolarization imagery from a geologic or ecologic perspective. An overview and summary of the system characteristics of the L-band synthetic aperture radar (SAR) flown on the NASA CV-990 aircraft are included as supplementary information. Other topics ranging from phase imagery and interferometric techniques to classifications of specific areas, and the potentials and limitations of SAR imagery in various applications are discussed.

CONTENTS



 

Tables

# PART I

# INTRODUCTION

# and

# SAR OPERATIONS OVERVIEW

# PROGRAM OVERVIEW AND WORKSHOP SUMMARY

D. N. Held

Jet Propulsion Laboratory

The NASA/JPL CV-990 L-band synthetic aperture radar (SAR) started producing digitally correlated, multiple polarized images in December 1983. Since then more than 200 images have been produced to service an ever-growing user community representing universities, government agencies, NASA centers, and JPL. In Fiscal Year 1985 we are committed to fly approximately 32 flights (see Figure 1) for over 25 users and to generate in excess of 160 image products. We are expecting the demands upon this system to grow substantially over the next few years since it is the prototype for SIR-C and the SAR system under consideration for the Earth Observing System (EOS). The radar, which currently generates four coregistered polarized images at L-band, is being upgraded to include C-band over the next year, and it is hoped that it will ultimately be capable of producing four polarized images at each frequency simultaneously, as will SIR-C.

The NASA/JPL Aircraft SAR Workshop was first conceived of as a small working group consisting of users and JPL engineers getting together to educate one another. It ultimately mushroomed into a rather large assemblage rivaling some of the larger international remote sensing conferences. The agenda for the Workshop is included as an Appendix to this report, as is a list of attendees.

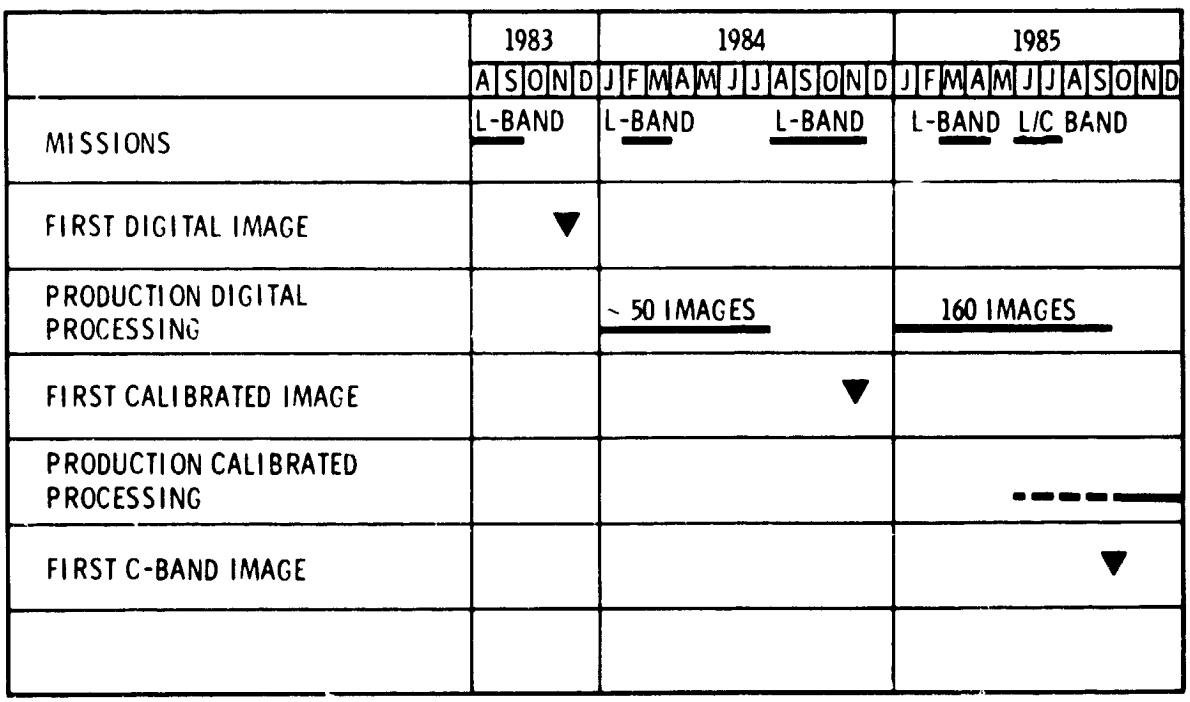


Figure 1. Overview of NASA/JPL CV-990 SAR program.

The original purpose of the Workshop was to acquaint the user community with the CV-990 SAR's capabilities, but it ultimately resulted in a forum wherein users presented preliminary results of experiments that were conducted with data acquired during the last year. Summaries of these talks, along with some preliminary material outlining the capabilites and operations of the L-band SAR, constitute the bulk of this Workshop Report.

At the end of two days of meetings, a summary session was held to elicit recommendations from the group in an effort to improve the future scientific yield of the program. These recommendations are listed below.

- STANDARDIZE, CATALOG, AND CALIBRATE ALL DATA PRODUCTS
- DOUBLE THE VOLUME OF DIGITAL DATA PROVIDED PER FLIGHT HOUR
- INCREASE UNIVERSITY PARTICIPATION IN THE PROGRAM
- PERFORM CORROBORATING LABORATORY SCATTERING EXPERIMENTS
- HOLD ANOTHER WORKSHOP LATE IN FY 1986

# RADAR SYSTEM DESCRIPTION

D. N. Held and W. E. Brown

Jet Propulsion Laboratory

This section contains a brief overview of the hardware and software utilized to generate the CV-990 SAR's image products. We shall first discuss the on-board hardware, then the operational processing software, and finally end with a description of the image products that are routinely available.

## Flight Hardware

The NASA/JPL CV-990 L-band SAR is an extremely versatile sensor capable of providing calibrated multiple polarization imagery of a wide variety of targets. One key to the flexibility of the system is the CV-990 aircraft itself, which has a very large operating range and a high cruising altitude. and is therefore generally unaffected by weather conditions over the target area (see Appendix A and Figure 2).

The sensor itself has a single transmitter and two identical receiver chains which are attached to a single strip line dual-polarized antenna (see Figure A-1). Thus it is possible to transmit on one polarization and subsequently receive and record the return echo in two polarizations simultaneously. It is also possible to switch the transmitter from one polarization to another rapidly such that, if the the pulse repetition frequency (PRF) is high enough, we can simultaneously acquire 4 polarization data (see Figure A-1).

Another feature of the radar system is the continuous injection of a calibration tone into both receiver channels. The level of this tone is carefully monitored by the system, and it serves as a means for calibrating the entire receiver chain and the digital correlator.

Finally the entire on-board sensor system is controlled and monitored by a Hewlett-Packard 9000 microcomputer which annotates the raw data as well as provides a very complete hard copy of all radar and aircraft parameters.

(a)

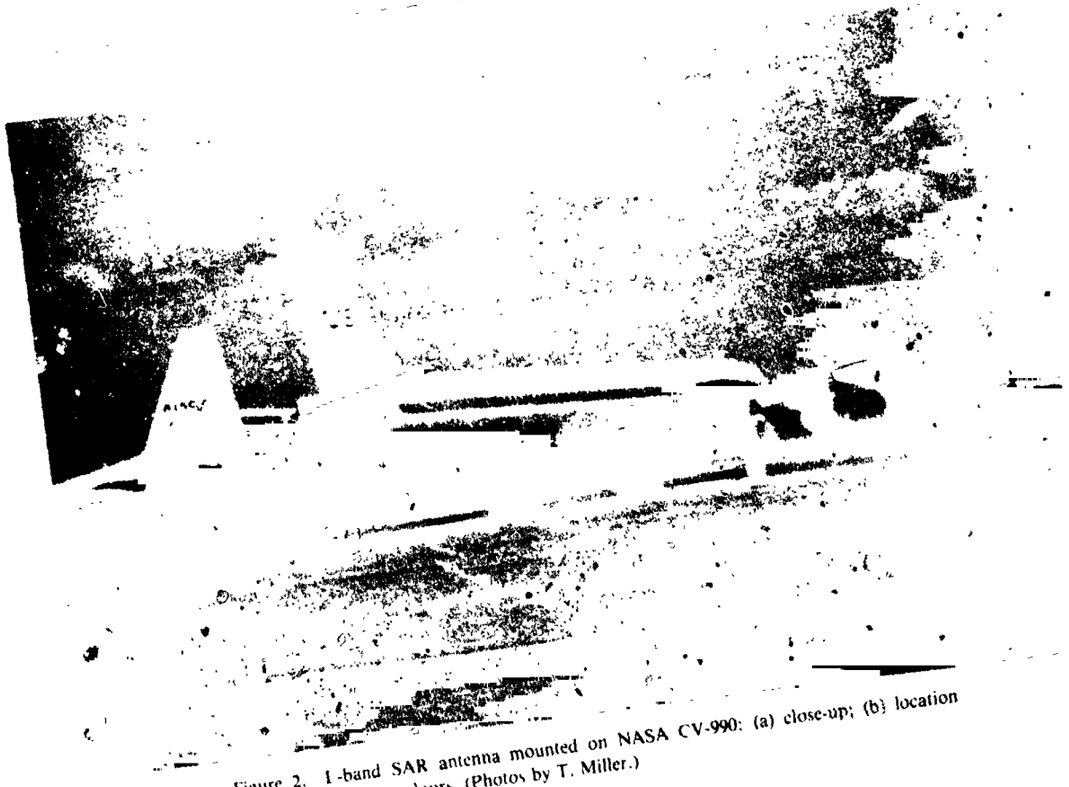

Figure 2. L-band SAR antenna mounted on NASA CV-990: (a) close-up; (b) location between rear baggage doors. (Photos by T. Miller.)

## Digital Processing Software

Once on the ground, the raw SAR data is played back into a VAX 11/780 computer system which, assisted by several 470 Mbyte disks and an array processor, can process several images each night. Annotation multiplexed into the SAR data stream by the sensor is utilized to configure the processor and the entire operation is largely automatic and operator independent.

The data is initially presummed (a coherent low pass filter) by a factor of eight to reduce its volume and then range and azimuth compressed, forming four coregistered images. When the radar is in its quadpolarization mode, these images will represent the following polarization combinations: HH (horizontal-transmit, horizontal-receive), HV, VH, and VV. The resulting imagery has approximately 4 million complex pixels per polarization which are stored in floating point format for further processing. To generate an intensity image of a particular polarization, the complex image is incoherently low-pass filtered in azimuth yielding a 4 look image with approximately one thousand real pixels on a side (see Appendix A).

A novel way of combining two polarizations (generally HH and VV) is to look at the phase difference on a pixel-by-pixel basis in the complex image and then subsequently low pass filter this data into a 1024 x 1024 real format. This "phase difference" imagery is now being produced routinely by the CV-990 SAR system and some of the papers presented at the Workshop address this type of image product.

## Image Products

There are several standard image products generated by a single correlation of a particular scene. First, floating point versions of the four 4-look images, as well as a floating point version of the phase difference image, are stored in the JPL aircraft radar data archive. From this data base a tape is prepared for submission to a DICOMED film recorder facility here at the Lab. The "DICO" tape contains a scaled 8-bit version of the original floating point data complete with the appropriate scale factor visible within the header block of the image.

Each of the four 4-look polarization images results in the generation of an individually scaled black-and-white hardcopy image. In addition, three of the four polarization images ( generally HH, VV, VH) are combined into a single false color image by assigning one polarization to each of three colors (red, blue, and green), and generating a color hard-copy image (see Figure 3). Finally, a hard-copy image is generated from the phase difference data by assigning a color table that results in the phase difference between the HH and VV data being perceived as the color of the image, and the intensity of the data being perceived as the intensity of the image. Figure 4 contains several examples of these "phase difference" images which are now routinely produced and disseminated.

Figure 3 (opposite page). Three intensity images of the different polarizations are combined into one color image by assigning each a different additive color This "color composite" image facilitates relative brightness comparisons between the different polarizations.

Figure 4 (following). Examples of phase difference imagery over various terrains. In these images, color represents the phase difference HH and VV returns, while brightness represents backscatter amplitude.

ORIGINAL PAGE
COLOR PHOTOGRAPH

COLOR COMPOSITE SAR IMAGES
DEATH VALLEY, CALIFORNIA

LHH

LHV

LVV

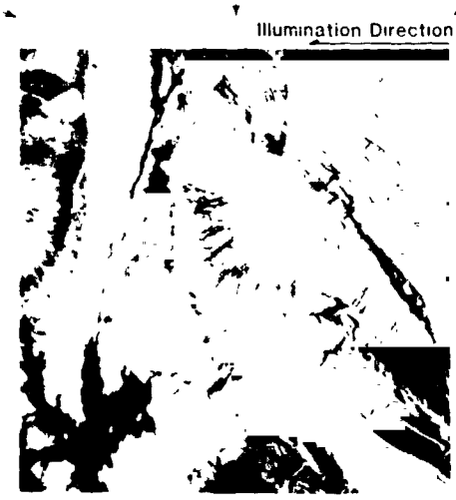

# EXAMPLES OF PHASE DIFFERENCE IMAGERY

**MINA, NEVADA**

Little or no vegetation. Zero degree phase difference except in the town.

**MACOMB, ILLINOIS**

Distinct phase difference Signatures corresponding to agricultural region

**MEDICINE LAKE, CALIFORNIA**

A variety of surfaces including bare lava and forested regions.

**WINCHESTER, VIRGINIA**

Phase "noise" Typical of multiple scattering in forested region.

# NASA/JPL AIRCRAFT SAR OPERATIONS OVERVIEW

T. W. Thompson

Jet Propulsion Laboratory

Since 1981 there have been several substantial upgrades of the NASA/JPL Aircraft L-band Synthetic Aperture Radar (SAR). These include control of the radar via a desk-top HP-9845 computer as well as digital recording and correlation of simultaneous HH, HV, VV, VH radar echoes. These improvements have become available to users via an operational setup based in large part upon the NASA/OSSA Applications Aircraft Program, the NASA/Ames Medium Altitude Missions Branch and their CV-990 aircraft.

An overview of this operation is shown in Figure 5. The first step for the user is to initiate an RTOP/Flight Request which is submitted to NASA Headquarters and the Applications Aircraft Program Office at NASA/Ames. If this RTOP/Flight Request is accepted, then a mission of several aircraft flights will be defined jointly by the NASA/Ames Medium Altitude Mission Branch, the users, and T. Thompson of JPL. Starting about two months before a flight series, aircraft hardware will be prepared for flight operations, and potential flight lines will be defined via user interactions with T. Thompson of JPL. This results in a premission flight plan which will be used during the mission for defining flight plans on a daily basis. This premission flight plan is also stored as a data matrix in the HP-9845 computer for identification of data during flight operations.

Real-time (flight) operations are conducted on a day-to-day basis during the mission. Users should participate on those flights, which include his or her data legs. Generally, a flight plan is generated on the day prior to the flight using the premission data matrix. This flight plan is used by a number of people on the CV-990 during the flight. The output for a flight includes raw SAR optical and digital data, supporting logs as well as CV-990 photography and ADDAS printouts and computer tapes. The raw SAR data is shipped to JPL for processing into products.

Postmission SAR processing at JPL is carried out in two steps: the production of survey optical prints in the form of strip contact prints (SCP's) followed by the production of digital images. Generally, users will select areas for digital correlation from the survey optical prints. Digital images will be produced based on a target latitude and longitude and a data leg identifier. Digital image output to the users (which is concurrently archived in the JPL Radar Data Center) includes IPL photographs and "DICO" computer compatible tapes.

The user is an integral part of these aircraft data acquisitions. He or she should (1) submit a RTOP/Flight Request, (2) define data legs about 2 months prior to a mission, (3) participate in the flights themselves, and (4) provide inputs for digital processing of the SAR images. The user can acquire high quality terrestrial radar data with this relatively simple operational setup.

 

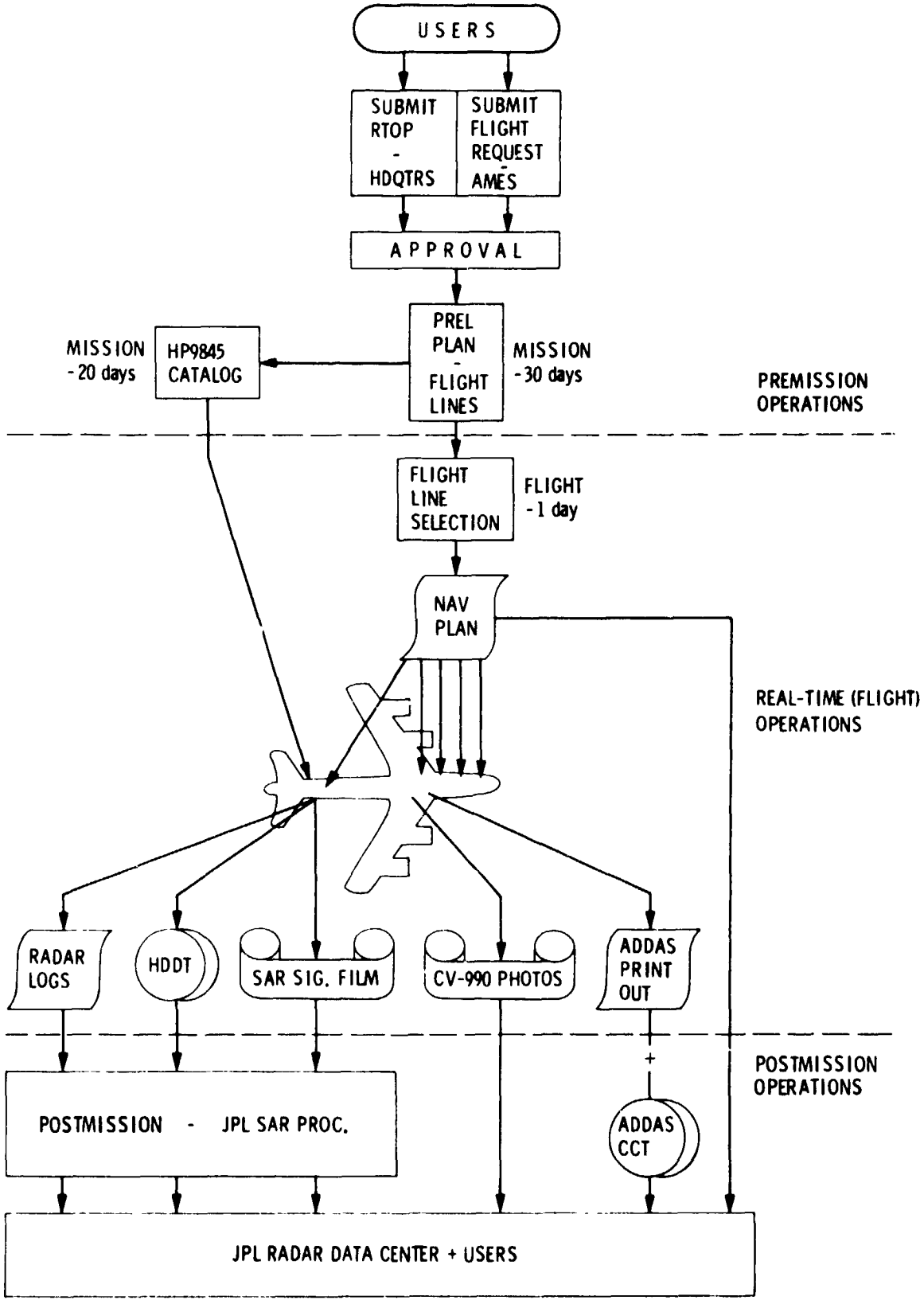


Figure 5. NASA/JPL aircraft SAR: operations overview.

# PART II

## SUMMARIES OF TALKS

# CV-990 L-BAND SAR: A CALIBRATION EXPERIMENT

D. N. Held and C. Werner

Jet Propulsion Laboratory

Calibrated image data is required by most users of synthetic aperture radar (SAR) data particularly those attempting to classify targets based upon their radar backscatter signature as a function of frequency polarization or incidence angle. In this experiment, we compare the backscatter derived by calibrating the NASA/JPL CV-990 L-band SAR, and the backscatter reported from a pass of the NASA/JSC C-130 scatterometer as the two instruments flew over the same site at different times.

The L-band SAR imagery was corrected for known systematic effects peculiar to the sensor hardware, and for the gain of the digital processor. The imagery was also corrected for the variation of slant range and ground range resolution across the swath. The resulting image data have the units of "sigma-zero" (a measure of radar cross-section) and are therefore directly comparable to data generated by the NASA/JSC C-130 scatterometer, which produces 1-dimensional tracks across a particular scene. For each point along the track, the scatterometer generates a curve of sigma-zero as a function of incidence angle. The SAR, on the other hand, produces only a single estimate of the radar cross section of a particular point on the ground, albeit at a known incidence angle. Thus if both instruments have scanned the same point on the ground, the scatterometer estimate of the backscatter can be directly compared with the SAR estimate.

Two SAR passes across Pisgah Crater in southern California, taken in 1984, were compared with a single scatterometer pass taken some four years earlier. One of the SAR passes was arranged to be parallel to the flight track of the previously flown scatterometer so that the scatterometer track appears at a constant slant-range (and incidence angle) in the SAR image. The other SAR pass was flown at an angle to the scatterometer so that the slant range (and incidence angle) track would vary as a function of time (see Figure 6). Unfortunately, these particular geometries do not make it possible to maintain parallel look-directions since the SAR is side-looking, and the scatterometer looks behind it. Thus if the targets are azimuthally anisotropic each sensor will measure a somewhat different backscatter even if perfectly calibrated.

The HH polarized image generated by the SAR was compared with the HH polarized data produced by the scatterometer and there appears to be a very high degree of correlation. In fact, the correspondence between the two sets of estimates is quite remarkable particularly when the time between the two observations and the difference in look-directions are considered. The data suggests that there is approximately a 2.5 dB systematic difference between the estimates generated by the two sensors.

In a previously reported result (Held, et al., 1983), calibrated Seasat SAR imagery of the same test area taken in 1978 was compared with the aforementioned scatterometer data yielding estimates that agreed with the scatterometer to within about 1 dB. Therefore, we are able to state that three entirely different active microwave sensors (two on airplanes and one in space), viewing the same target on three separate occasions, were able to agree with one another on a pixel-by-pixel basis to within approximately 2.5 dB. This is not quite the same as saying that all three instruments are absolutely calibrated within 2.5 dB; however, it is most certainly a very encouraging and landmark result.

The results reported above apply to the HH polarization ONLY. However, they can reasonably be assumed to apply to the VV polarization as well. The results ARE NOT REPRESENTATIVE of the calibration accuracy of either of the cross-polarized images: HV and VH. This is due to cross talk between the polarizations which occurs principally in the antennae but also, to some extent, in other parts of the radar. The calibration of this cross talk and the production of 4 calibrated images from the raw data are continuing subjects of research.

## REFERENCE

Held, D., C. Werner, and S. Wall, 1983. "The Absolute Amplitude Calibration of the SEASAT Synthetic Aperture Radar," International Geoscience and Remote Sensing Symposium, San Francisco.

Figure 6. A high degree of correlation between the 1984 L-band SAR backscatter returns and the 1980 scatterometer flight over the same area (this flight is indicated by the white track across the SAR images) can be seen in spite of the time delay. This supports the current calibration approach.

ORIGINAL PAGE IS
OF POOR QUALITY

# TWO AIRCRAFT PASSES OVER PISGAH

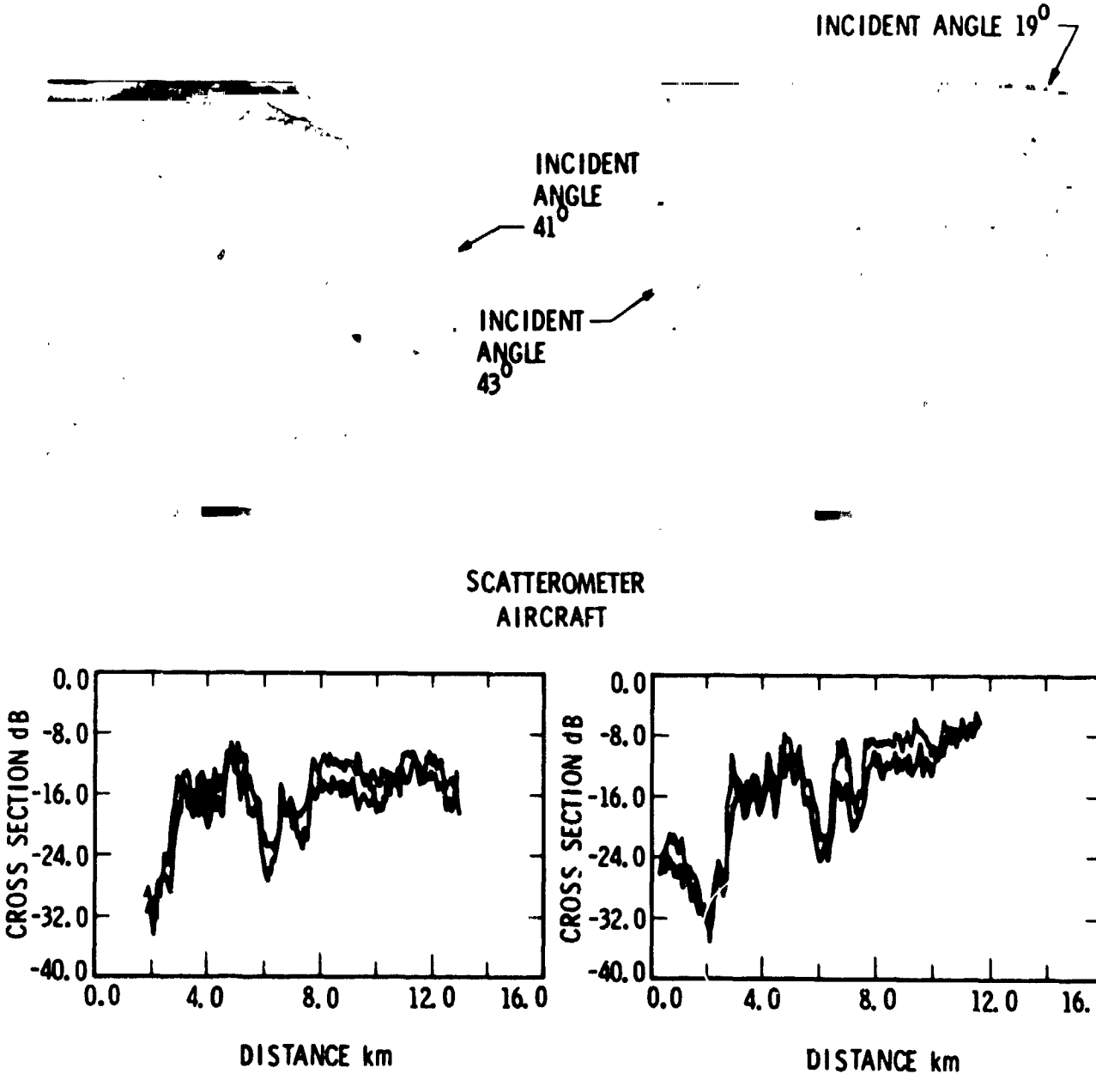

# NEOGENE COMPRESSIONAL DEFORMATION AND POSSIBLE THRUST FAULTING IN SOUTHWEST DOMINICAN REPUBLIC

M. P. Golombek, P. Goreau, and T. H. Dixon

Jet Propulsion Laboratory

Analysis of regional and high resolution remote sensing data coupled with detailed field investigations indicates Neogene compressional deformation in the southwest Dominican Republic. Airborne synthetic aperture radar data (Figure 7) and high resolution near infrared photography show folds in Tertiary sediments and possible thrust fault scarps implying NE-SW compression in the region. Large road cuts through the scarps allow study of otherwise poorl accessible, heavily vegetated karst terrain. Deformation increases toward scarp fronts where small bedding-plane thrust faults become more numerous. Analysis of mesoscopic faults with slickensides indicates compression oriented between N-S and E-W. The lowermost scarp has highly sheared fault breccia and undeformed frontal talus breccias implying it is the basal thrust into which the higher thrust faults sole. Thus the scarps probably formed in a regional NE-SW compressional stress regime and are the toes of thrust sheets. Previous workers have suggested that these scarps are ancient shorelines. However, the gross morphology of the scarps differs substantially from well known erosional terraces on the north coast.

Some compression in north and central Dominican Republic is expected due to transpression in the left-lateral shear system associated with motion between the Caribbean and North American plates. However, the scarps discussed here in the southernmost part of the island and previously reported offshore data indicating thrust faulting as far south as the Beata Ridge indicate significant compressive stresses at great distances from the transform. This compression implies some component of convergence between the Caribbean and North American plates.

Figure 7. Dominican Republic: optically correlated L-band airborne SAR near- and far-range mosaic Flight dates: 820722 and 820724.

N86-10619

# THE EFFECT OF VEGETATION TYPE, MICRORELIEF, AND INCIDENCE ANGLE ON RADAR BACKSCATTER

Manfred Owe, Peggy E. O'Neill, Thomas J. Jackson, and Thomas J. Schmugge

Goddard Space Flight Center

The NASA/JPL SAR was flown over a 20 x 110 km test site in the Texas High Plains regions north of Lubbock during February/March 1984. The area is agricultural in nature, consisting of both dry land and irrigated fields, primarily in wheat, alfalfa, corn and cotton, as well as grazed and ungrazed rangeland of varying vegetation density. As the experiment was conducted early in the year, cultivated fields were either freshly tilled, fallow bare, covered with stubble from the previous season or in winter wheat. The quad-pole SAR imagery was taken in conjunction with passive microwave measurements as part of an experiment to observe the spatial variation of surface soil moisture within the test site.

Unfortunately, the range of surface moisture was insufficient to detect an observable change in the radar, based on variation in soil moisture alone. The average surface soil moisture throughout the test site was below 10 percent. By essentially eliminating a potentially highly variable parameter like soil moisture, the experiment afforded a unique opportunity to observe the relationship between the radar signature and various noise sources such as incidence angle and surface physical characteristics, i.e., vegetation and surface roughness.

Color composite photographs using the VH, VV, and HH pole configurations (Figure 8) were viewed and compared to both ground truth data and color infrared photography. A variety of features that could not be detected on the infrared photo were visible on the radar image, although the converse was found to be true in some cases as well. The SAR image readily distinguished individual cultivated fields and range lands, due to highly contrasting backscatter from the varying surface conditions. Linear metallic features, such as fences, power lines, and center pivot irrigation rigs, appeared as exceptionally bright targets when oriented parallel to the line of flight. Metallic farm buildings also exhibited bright returns, as did certain fields and cover conditions, and so could be distinguished from each other only by virtue of identification on the color IR photo.

The effect of incidence angle was investigated by comparing the pixel values of the calibrated and uncalibrated images. Ten-pixel-wide transects along the entire azimuth were averaged in each of the two scenes, and plotted against the calculated incidence angle of the center of each range increment. It is evident from the graphs that both the magnitudes and patterns exhibited by the corresponding transect means of the two images are highly dissimilar. For each of the cross-poles, the uncalibrated image displayed very distinct and systematic positive trends through the entire range of incidence angles. The two like-poles, however, exhibited relatively constant returns. In the calibrated image, the cross-poles exhibited a constant return, while the like-poles demonstrated a strong negative trend across the range of look-angles, as might be expected.

Two classification analyses were performed with the calibrated data. First, the scene was subdivided into quarter-section parcels (0.6 $km^2$). The pixel values for each band were subsequently averaged within each quadrant. It was noticed in many instances that the excessively bright return from fences and powerlines tended to bias the quadrant means beyond recognition. This problem was overcome by excluding a ten-pixel border around each quadrant prior to averaging. A cluster analysis was then performed on the resulting 130 quadrants (Figure 9). Quadrants were clustered very accurately when compared to the color composites, but less so when compared to the observed ground truth. In many instances where the radar signatures of different surfaces are similar, it is not necessarily essential to differentiate between the surfaces. In other cases, though, it is very important, especially if the hydrologic characteristics of the surfaces are vastly different.

An additional classification analysis was performed on the entire image. Clusters were combined and reduced to seven distinct classes. The classified image closely resembled the color composites, but again some misclassification was observed. It was noticed that fields with similar surface characteristics would exhibit similar radar returns in the cross-poles going from the near to the far range, but would often have significantly lower values in the two like-poles. The relative difference between the VV and HH poles was still similar. Surfaces which appeared exceptionally bright at the near range (the result of deep-furrowed north/south tilling) were found to be as dark at the far range as smooth, freshly disked fields in the near range. This phenomenon was most pronounced in the two like-pole returns.

Active microwave systems have demonstrated potential in detecting spatial variation in surface soil moisture. It has also been shown that soil roughness and vegetative cover are key noise parameters that affect the characteristic radar return from the soil surface. Because of this sensitivity to surface condition, SAR can be an excellent component of a multisensor imaging system. But, to be of maximum utility, greater standardization in the processing of the imagery must be achieved, both within and between missions, while some standardized calibration procedures need to be implemented.

Figure 8. This color composite SAR image readily distinguishes individual cultivated fields and range lands because of the highly contrasting backscatter from the varying surface conditions.

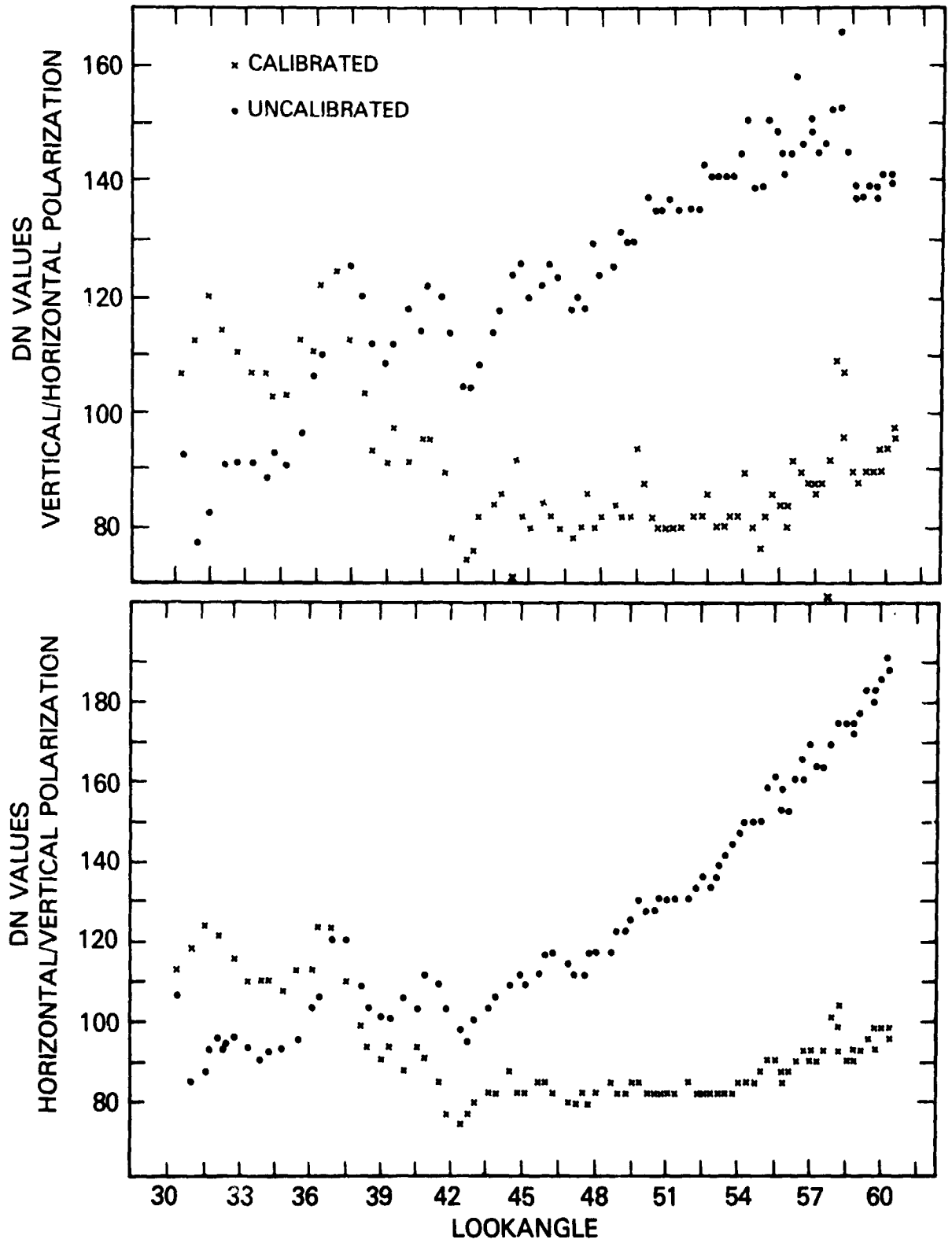


Figure 9. A comparison of calibrated and uncalibrated quadpole radar returns.

# AGE-DATING VOLCANIC AND ALLUVIAL SURFACES WITH MULTIPOLARIZATION DATA

Tom G. Farr

Jet Propulsion Laboratory

The surfaces of lava flows and alluvial fans tend to become smoother with age as the processes of physical and chemical weathering and aeolian deposition combine to reduce the sizes of rock projections and fill in low spots. The rate at which these surfaces smooth is a function of rock type and climate, suggesting that if something is known about these parameters, measurements of microrelief can be used to age-date volcanic and alluvial surfaces. Since the response of radar sensors to geologic surfaces is proportional to the microrelief of the surfaces, radar image brightness should be a function of the age of a surface, provided rock type and climate are relatively constant.

JPL aircraft multipolarization radar images of alluvial fans in the Owens Valley and lava flows of the Cima Volcanic Field, California, were obtained in spring and fall, 1984. Both areas have been well mapped and ages have been determined for many of their surfaces. The climate in the areas is semi-arid at present, although wetter climates in the past have been responsible for significant modification of the surfaces.

The alluvial fans of the Owens Valley are dominated by granitic rock types derived from the Sierra Nevada Mountains to the west. Younger surfaces in this area are dominated by boulders up to 1 meter in diameter. There is little soil development other than a sandy regolith generated by granular disintegration of the boulders. Older surfaces gradually develop soil which fills in low areas between boulders, eventually submerging them. Vegetation on the surfaces varies with age; however, radar images of burned areas indicate that native vegetation plays only a minor role in the radar backscatter from the surfaces in Owens Valley.

A false-color multipolarization version of one of the images of the Owens Valley area acquired by the JPL SAR is shown in Figure 10. A geologic map of the alluvial fans there (Gillespie, 1982) is also shown for comparison. In general, brightness in the multipolarization images can be seen to be inversely proportional to the age of the surfaces. A more detailed investigation of the relationship between backscatter and age of the surfaces was undertaken with calibrated aircraft SAR data. Figure 11 shows the quantitative relationship between backscatter coefficient and age for the three polarizations. The straight lines connecting the measured data points imply a steady-state process, although the process or processes leading to this relationship may have operated at rates that varied with climate fluctuations, such as the glacial ages.

Work in the Mojave Desert region by Dickey et al. (1980) and Wells et al. (1984a) has shown that variations in rates of geomorphic processes have been

 

consistent over a large area for the last several hundred thousand years. The Cima Volcanic Field has recently been intensively studied as an area within which a variety of geomorphic surfaces could be dated through their relationships with lava flows that have erupted over the last million years (Dohrenwend et al., 1984a,b; Wells et al., 1984b). These papers describe the geomorphic evolution of cinder cones and lava flow surfaces, including factors such as surface roughness, which decreases with age through weathering of original roughness elements, and filling in of hollows by aeolian materials in episodes related to glacial ages. This same decrease can be seen as a decrease in brightness in aircraft SAR images taken of the field. Figure 12 shows a graph of the uncalibrated brightness values (DN) of flows of different ages in the Cima Volcanic Field.

It is expected that the relationship between radar brightness and age is a consistent one, and that with the wider availability of calibrated radar backscatter data, these relationships can be extended to less well-known areas. The effect of variables such as past climate fluctuations, tectonic disturbance, and rock type must be understood before extension beyond the Mojave Desert region can be attempted.

Figure 10. Age-dating alluvial deposits in Owens Valley, California: a false-color three-polarization aircraft SAR image obtained on September 28, 1984, showing alluvial fans (center) derived from the Sierra Nevada Mountains (left). Different fan units are relatively homogeneous areas bounded by bright stream beds. Geologic map for comparison with SAR image; fan units of different ages are shown.

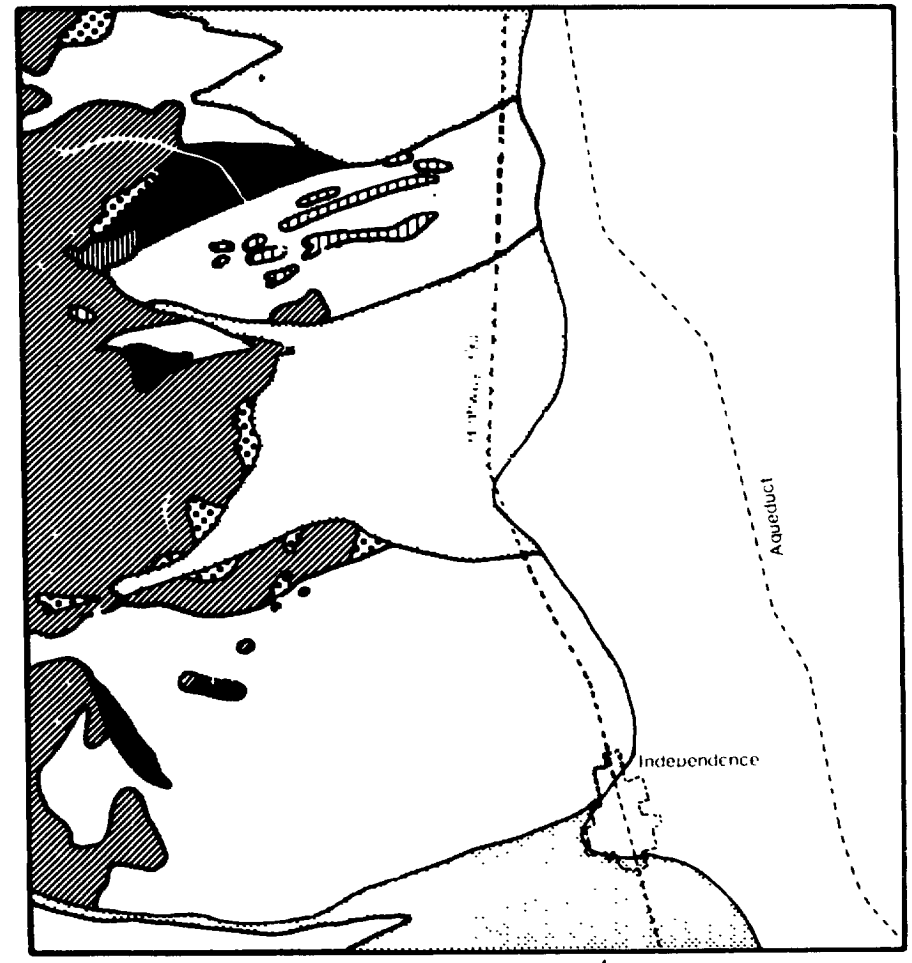


EXPLANATION

Holocene
- Alluvium
- Colluvium

Pleistocene
- Young Fan
- Old Fan
- Basalt
- Very Old Fan
- Basalt
- Bedrock

N

Illumination Direction

1 km

Gillespie, 1982, Ph.D. dissertation.
California Institute of Technology

Red = LVV
Green = LHH
Blue = LHV

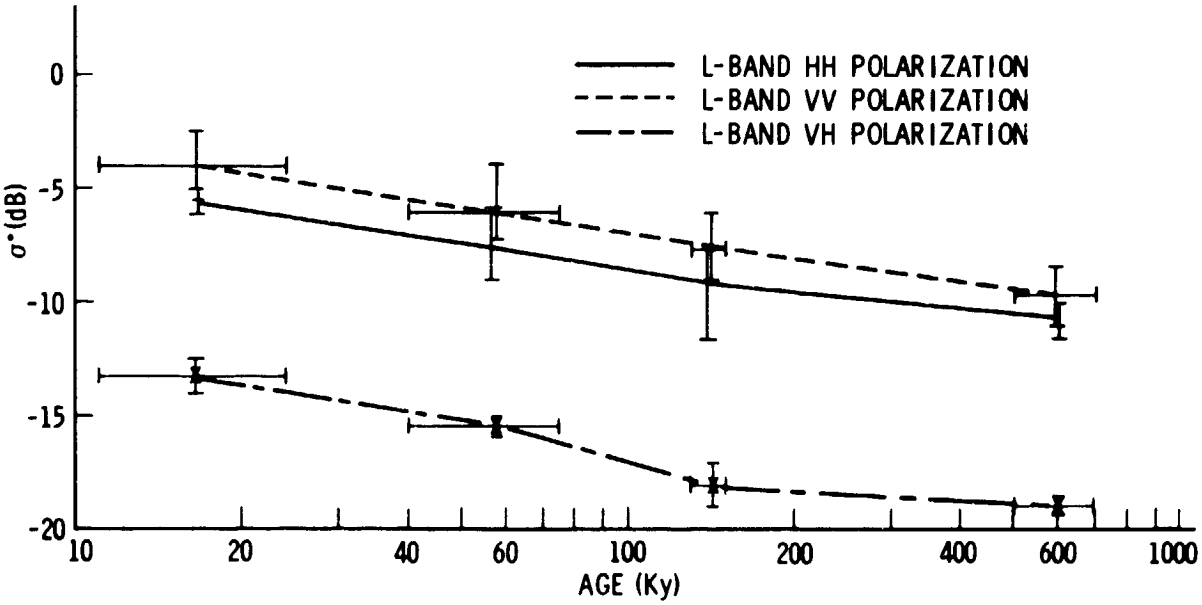


Figure 11. The relationship between calibrated aircraft multipolarization SAR image data and alluvial fan ages in Owens Valley. Bars indicate the standard deviation of backscatter values and range of ages attributed to glacial ages responsible for fan units.

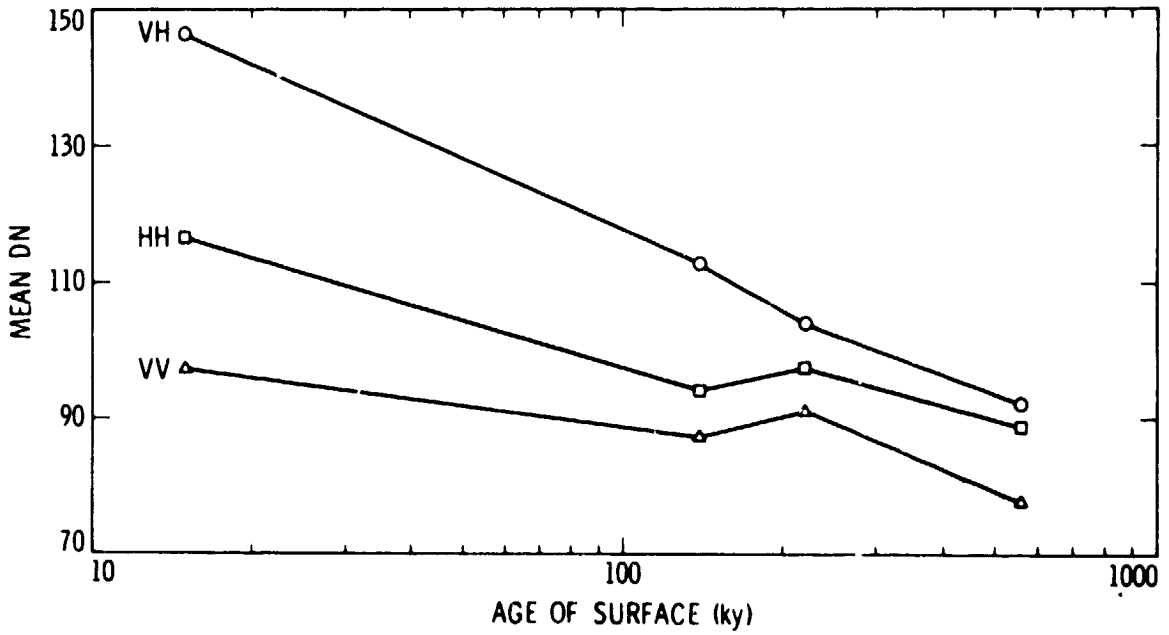


Figure 12. The age-brightness relationship for lava flows of the Cima Volcanic Field, California. KAr ages are from Dohrenwend et al. (1984a).

## REFERENCES


Dickey, D. D., W. J. Carr, W. B. Bull, 1980, Geologic map of the Parker NW, Parker, and parts of the Whipple Mountains SW and Whipple Wash quadrangles, California and Arizona, U.S. Geological Survey Map I-1124.

Dohrenwend, J. C., ed., 1984, Surficial Geology of the Eastern Mojave Desert, California, Guidebook, Geol. Soc. Amer., Ann. Meeting, Reno, NV, November, 1984.

Dohrenwend, J. C., L. D. McFadden, B. D. Turrin, S. G. Wells, 1984a, K-Ar dating of the Cima volcanic field, eastern Mojave Desert, California: Late Cenozoic volcanic history and landscape evolution, Geology, Vol. 12, p. 163-167.

Dohrenwend, J. C., S. G. Wells, B. D. Turrin, L. D. McFadden, 1984b, Rates and trends of late Cenozoic landscape degradation in the area of the Cima volcanic field, Mojave Desert, California, in Dohrenwend, 1984.

Gillespie, A. R., 1982, Quaternary glaciation and Tectonism in the Southeastern Sierra Nevada, Inyo County, California, unpublished Ph.D. thesis, California Institute of Technology, Pasadena, CA, 695 pp.

Wells, S. G., L. D. McFadden, J. C. Dohrenwend, T. F. Bullard, B. F. Feilberg, R. L. Ford, J. P. Grimm, J. R. Miller, S. M. Orbock, J. D. Pickle, 1984a, Late Quaternary geomorphic history of Silver Lake, eastern Mojave Desert, California: An example of the influence of climatic change on desert piedmonts, in Dohrenwend, 1984.

Wells, S. G., J. C. Dohrenwend, L. D. McFadden, B. D. Turrin, K. D. Mahrer, 1984b, Types and rates of late Cenozoic geomorphic processes on lava flows of the Cima volcanic field, Mojave Desert, California, in Dohrenwend, 1984.

N86-10621

# THE EFFECTS OF MERGING TM AND A/C RADAR ON WETLAND CLASSIFICATION

James P. Ormsby and Patricia J. Mulligan

Goddard Space Flight Center

The process of monitoring changes within a wildlife area is often hampered by inaccessibility. Efforts to provide better information to manage and maintain the viability of a wildlife refuge through the use of remote sensing are being studied. Using visible and near-IR data one must rely on spectral differences of vegetation to separate flooded forest areas from upland areas or detect the land-water boundary. In forest regrowth areas the species mix may not change making separation difficult. Also, in some cases during the growing season the water surface can be obscured by floating vegetation. Improved subdivision in the classification of forested wetlands has been achieved through the merging of Landsat Multispectral Scanner (MSS) and Seasat SAR (Wu, 1980). Radar systems offer a means for mapping both interior and coastal wetlands as well as monitoring flood conditions (Waite et al., 1981). Benton et al. (1983) and Ormsby et al. (1985) discussed the benefits of using multifrequency microwave data (L-, C-, and X-band) along with color infrared (CIR) and Landsat data. While radar does not provide detailed vegetation discrimination, it will provide the means to separate areas of different moisture conditions (Benton, 1983) - thus, the use of Landsat Thematic Mapper (TM) in conjunction with the microwave data. If successful, information on shoreline cover, emergent wetland vegetation and extent, and submerged grassbeds would provide much needed data for planning and maintenance of wetlands.

The Blackwater Wildlife Refuge, located on Maryland's Eastern Shore, consists of open waterways, marshes, backwater areas, and a small amount of upland forest. A study area within this refuge, the U.S.G.S. 7-1/2 minute quadrangle of 'Golden Hill', was chosen because it includes portions of all of these as well as agricultural land. The wildlife refuge provides the ideal opportunity because of variable water conditions and plant species as well as the excellent cooperation, interest, and assistance provided by the rangers.

Originally, the goal was to determine the accuracy with which one could categorize various types of vegetation and land use within an inland wetland using Landsat TM data. First, a Level I/II supervised classification was performed. Following a more detailed ground truth survey, a Level III classification was done. Aircraft L-band radar data were received and the decision was made to merge the TM and L-band data and assess whether vegetation categories within the wetland areas could be better defined.

The TM data were obtained from the November 2, 1982, scene of the Washington, D.C., Baltimore, and Chesapeake Bay areas. An area larger than the Golden Hill quad was extracted for analysis. High altitude aerial CIR photography taken in 1981 and low altitude (243 to 610 meters (800 to 2000 feet)) true color photography surveying the Golden Hill site in 1984 were used for photointerpretation of ground cover.

The SAR data were acquired on 3 March and 16 September 1984. Strong upper winds (over 31 m/s (70 mph)) hampered data acquisition during the March flight. Flight lines parallel to the upper winds (east-west) were requested for the September data.

Upon receipt of the March quick-look data JPL personnel were given information on the location of the required subsets for digital processing. The high drift angle (+7 degrees) needed to maintain flight position during the March flight resulted in data of questionable quality; ghosts and other aberrations could be found throughout the images. To acquire sufficient data in a single image to overlay the Golden Hill quad four subscenes had to be mosaicked. The use of different scaling factors for each subset produced a radar image looking like a patchwork quilt. An attempt was made to normalize the data based on the scaling factors used on the four subsets (Thompson and Donovan, 1984). This did not alleviate the problem. After discussions with JPL personnel it appears to be more involved. In addition, portions of adjacent subsets obtained from the same flight line were missing. The radar data, thus, when combined with the TM data for a supervised classification, showed no improvement in delineating various vegetation areas. In fact, the results were not as good as when the TM data were used alone.

For the September date quadpole data were available (Figure 13). Currently HH and VH ground range data are being merged separately and together with TM bands 3, 4, and 5 over a small portion of the quad. Preliminary results from the unsupervised classifications indicate vegetation delineation is improved for open agricultural areas and water, but other features are more confused. Once these and other problems are alleviated the potential for improved multispectral classification can be achieved.

## REFERENCES


Benton, Jr., A. R., A. J. Blanchard, and R. W. Newton, 1983. "Multi-frequency Radar Interpretation Techniques Applied to the Coastal Zone," 1983 ASCM-ASP Fall Convention, Salt Lake City, Utah.

Ormsby, J. P., B. J. Blanchard, and A. J. Blanchard, 1985. "Detection of Lowland Flooding Using Active Microwave Systems," to be published in Photogrammetric Engineering and Remote Sensing.

Thompson, T. W. and N. Donovan, 1984. Personal Communication.

Waite, W. P., H. C. MacDonald, V. H. Kaupp, and J. S. Demarcke, 1981. "Wetland Mapping with Imaging Radar," International Geoscience and Remote Sensing Symposium (IGARSS'81) Digest Vol. 2. p. 794-799.

Wu, S. T., 1980. "An Improvement in Land Cover Classification Achieved by Merging Microwave Data with Landsat Multispectral Scanner Data." American Society of Photogrammetry. Spring Meeting, St. Louis, MO, March 1980, p. 293-309.


Figure 13. In the HH and VV, although basically the same vegetation grows in near range as in far range, the brightnesses are quite different. Because of changes in gains and geophysical parameters as well as the scaling factors used in displaying the image, the author was unable to use this data separately or in combination with other data (e.g., TM) in land cover discrimination studies.

N86-10622

# TOPOGRAPHIC MAPPING FROM INTERFEROMETRIC SYNTHETIC APERTURE RADAR OBSERVATIONS

Howard A. Zebker and Richard M. Goldstein

Jet Propulsion Laboratory

Radar-interferometric techniques have been utilized to remove the north/south ambiguity in Earth-based observations of Venus (Rogers and Ingalls, 1969), to measure lunar and Venusian topography (Zisk, 1972a; Zisk 1972b; Rumsey et al., 1974), and to observe interference fringes modulated by Earth topography (Graham, 1974). We report here our determination of high-resolution topographic maps derived from interferometric synthetic aperture radar observations of the Earth.

Topographic maps are typically determined from stereo-pair optical photographs (Manual of Photogrammetry, 1980). Vertical relief causes the same terrain to appear in a slightly different projection for differing look angles, and this shift in appearance is interpreted in terms of the height of the terrain. The radar interferometric approach is related to the stereo technique in that the terrain is viewed at two different angles; however, in our case, the angular separation of the antennas is extremely small, on the order of a milliradian or less, as compared to tens of degrees for the optical case. Thus, the geometrical distortion and subsequent rectification correction algorithms are much less severe in the reduction of interferometric data. Recently, stereo-pair radar imagery has also been used to produce topographic maps (Kobrick and Leberl, 1984); however, the methods used are extensions of the optical stereo technique rather than the interferometric approach described here.

We utilize data that were recorded using a side-looking synthetic aperture radar system mounted on a NASA CV-990 aircraft, and processed at the Jet Propulsion Laboratory using a digital data processor implemented in software on a general purpose VAX 11/780 computer. The radar and processor operating characteristics are summarized in Appendix A. We configure the airplane radar hardware such that a signal is transmitted by a single antenna mounted on the underside of the right wing of the aircraft; reflected energy from the ground is received by that antenna and simultaneously by a second antenna on the underside of the left wing. Data from each antenna is recorded and processed separately to yield two 10-m resolution complex (magnitude and phase) images of the illuminated terrain. Interference fringes are produced when these two data sets are combined point by point to obtain a single image whose phase at each location is the difference of the two original phases, and whose magnitude is the product of the two original magnitudes.

The radar instrument, as with most pulsed radar systems, yields the line-of-sight distance, or slant range $\rho$, from the antenna to the target (see Figure 14a). However, this distance is indeterminate within the slant range resolution of the radar, which depends principally on the transmitted signal bandwidth. For our system this uncertainty is approximately ±3.75 m. The interferometric technique permits in addition the determination of the distance $\rho - \rho'$ to much greater precision, typically to an accuracy of a

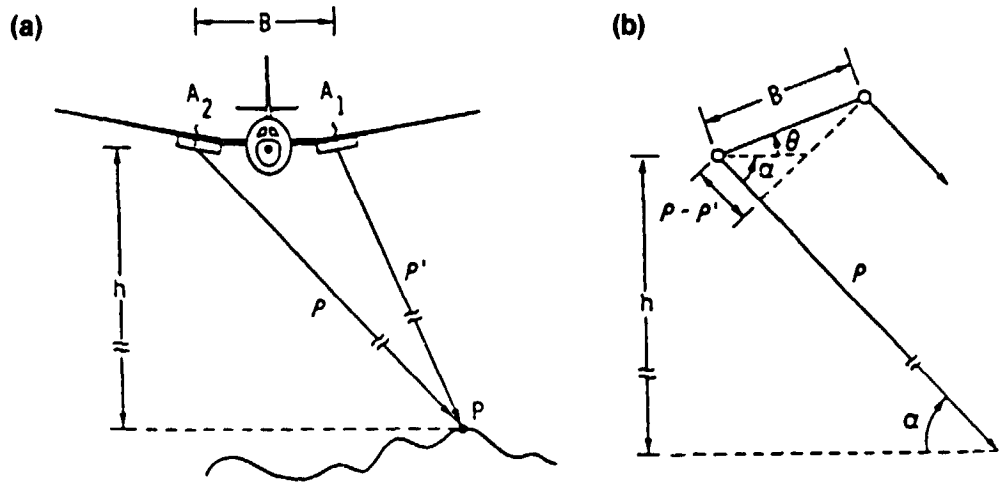


Figure 14. Radar interferometer geometry: observational geometry of the interferometer. A wave (a) is transmitted from antenna $A_1$ and is received simultaneously by antennas $A_1$ and $A_2$. Conventional radar measures the distance $\rho$ to an accuracy of $\pm 3.75$ m; interferometric technique permits, in addition, the determination of $\rho - \rho'$ to about 1 cm. These two measurements, with the geometrical factors B and r shown in detail in (b), are sufficient to find aircraft height h for each point in the radar image.

centimeter. Application of simple geometric identities then yields the vertical distance from the antennas to the surface. This measurement, when combined with the usual along-track and slant range measurements, yields the three-dimensional position of a given point in the image. Knowledge of the location of each point then permits rectification of the image to a cartographically accurate form.

We illustrate the observational geometry in more detail in Figure 14b. Two antennas, $A_1$ and $A_2$, separated by a baseline distance B, are mounted at an angle $\theta$ with respect to horizontal. For the aircraft system we used the angle $\theta$ at very nearly zero, but $\theta$ does change slightly as the aircraft rolls. The depression angle of an illuminated point is $\alpha$. The path difference $\rho - \rho'$ is thus related to these angles by

$$\rho - \rho' = B \cos (\theta + \alpha) \tag{1}$$

while the height h is

$$h = \rho \sin \alpha \tag{2}$$

The measured phase $\phi$ of the interference pattern at a point is the corresponding distance $\rho - \rho'$ in wavelengths, which expressed in radians is

$$\phi = (\rho - \rho') \cdot \frac{2\pi}{\lambda} \tag{3}$$

Combining (1), (2), and (3) we obtain an expression for h in terms of the observational geometry B, $\theta$ and the measurable quantities $\phi$ and $\rho$, as follows:

$$h = \rho \sin \left( \cos^{-1} \frac{\phi\lambda}{2\pi B} - \theta \right) \qquad (4)$$

We apply (4) to the interference image in order to determine the vertical distance to the antennas, which we combine with the along-track and slant range measurements to infer the three-dimensional location of each point. The data is then rectified to correct for geometrical distortions and interpolated to fit a square grid, resulting in a cartographically accurate map of the height of the illuminated terrain. The original radar amplitude image can be interpolated using the same height data, with the result that the topography and the radar reflectivity are now precisely correlated in position. This aids in interpretation of the radar brightness data itself.

Differentiation of (4) with respect to $\rho$, $\phi$, and $\theta$ yields the sensitivity of the height measurement to uncertainties in slant range, phase estimation, and antenna orientation, respectively. Typical values for airborne geometries yield a contribution to the overall error of about 3-4 m from each source, or roughly 6 m rms error.

Another type of error results from the $2\pi$ ambiguity associated with phase measurements; in other words, a phase measurement of x radians is indistinguishable from a measurement of $x + 2n\pi$ radians, where n is any integer. We overcome this problem by examining the data using an algorithm that is sensitive to phase differences in a two-dimensional field, and tracks the relative phase over the full image. We thus "unwrap" the ambiguous $2n\pi$ at each point to obtain a single-valued function valid over the entire image. This still leaves an absolute $2m\pi$ ambiguity, where m is an undetermined integer constant, which at present we remove using a priori knowledge of the true height at a single point in the image. The full interferometric data set is corrected for this absolute offset before applying (4) to determine the topographic map.

We assess the accuracy of the technique by comparison of a topographic image (Figure 15) with United States Geological Survey topographic maps of the same area; however, our interferometer data represent the most precise digital data available to us so it is difficult to determine the absolute accuracy. Contour maps are quite detailed and provide the best assessment of performance. At present only a preliminary comparison has been completed, but we have noted a considerable degree of coincidence between the two contour maps. We have also measured the standard deviation of the heights over part of an ocean region, which we can presume to be quite flat, and obtained a 6 m rms error. This is quite consistent with the above theoretical value. We hope to improve our verification technique in the future. However, we feel that the interferometric technique is a new, viable approach to the remote determination of topographic data.

## REFERENCES


Graham, L. C., 1974. Synthetic interferometer radar for topographic mapping, Proc. IEEE, June.

Kobrick, M., and F. Leberl (1984). Convergent stereo with the Shuttle Imaging Radar, submitted to Photo. Eng. and Rem. Sens.

Manual of Photogrammetry, 1980. Chapter 10, ed. C. C. Slama, American Society of Photogrammetry, Falls Church, VA.

Rogers, A. E. E., and R. P. Ingalls, 1969. Venus: mapping the surface reflectivity by radar interferometry, Science 165, 797-799.

Rumsey, H. C., G. A. Morris, R. R. Green, and R. M. Goldstein, 1974. A radar brightness and altitude image of a portion of Venus, Icarus 23, 1-7.

Zisk, S. H., 1972a. A new, Earth-based radar technique for the measurement of lunar topography, Moon 4, 296-306.

Zisk, S. H., 1972b. Lunar topography: first radar-interferometer measurements of the Alphonsus-Ptolemaeus-Arzachel region, Science 178, 977-980.


Figure 15. Here color correlates with altitude as determined from aircraft SAR interferometric earth observations. Note the uniform coloration of the virtually flat ocean.

# STRATEGIES FOR ANALYZING MIXED PIXELS IN REMOTELY SENSED IMAGERY

Milton Smith and John Adams

University of Washington

Two uncalibrated SAR scenes from Death Valley, California, and two uncalibrated scenes from Owens Valley, California, were used to test a technique to identify and separate the primary factors associated with multipolarized radar image sets. Unique to the technique is the concept that varied types of radar polarization signatures are a result of the interaction of a few physical factors (e.g., roughness, volume scattering, and dielectric constant). Thus, the varied signatures observed in an image reflect the interaction between these factors. In contrast to objectives that directly associate ground features to SAR polarization signatures, it is our objective to first separate the interaction of factors directly influencing the measurement. Secondly, we attempt to identify these factors. Interpretation of the SAR image sets proceeds by testing models that hypothesize the cause and effect relations between those factors directly affecting the radar measurement and those features of interest to the interpreter.

A goal of our approach is to separate and identify multipolarized radar endmember signature types. These endmember types are selected from a SAR image set by application of two constraints. First, the linear combinations of the endmember types must be capable of forming all other polarized signatures for each pixel. Secondly, the coefficients on each endmember type must lie within the range of 0 to 1. On each of the four SAR image sets used, we were able to separate four endmember types with a residual mean rms error of 2-3 DN values for each image. The residual mean rms error was computed by taking the difference between the prediction of each pixel in an image at each polarization using linear combinations of the endmember types and the measured DN value. This difference was then squared and summed over the four polarizations and then summed over the entire image. The square root of this value is the residual mean rms error.

The results of our analysis indicated two consistent endmember types over all four image scenes. These types are defined by a high flat polarized signature near a level of 255 DN and a low level flat signature near 0 DN for all polarizations. Four other endmember types were also isolated. The spatial distribution of these endmember types indicates possible correspondence to surface volume scattering and changes in surface dielectric. However, the shapes of these endmember types were different from scene to scene. This inconsistency may also result from the use of uncalibrated images or the compressed decibel scale.

Limited interpretation of color composites of the concentrations of endmember types for each image scene coincided with a logical interpretation of the surface structure. For example, regions of Owens Valley associated with low agricultural crops showed a mixture of endmember types associated with surface roughness and endmember types associated with volume scattering.

 

Areas with trees were associated with only the volume scattering endmember types. While further field checking is necessary, preliminary results indicate a partial separation and identification of factors directly corresponding to the multiple SAR polarizations.

N86-10624

# LITHOLOGIC MAPPING IN A SEDIMENTARY ENVIRONMENT USING MULTIPOLARIZATION SAR IMAGES

Diane Evans and Leslie Schenck

Jet Propulsion Laboratory

Multipolarization SAR data from the NASA/JPL aircraft SAR have been used in conjunction with Landsat Thematic Mapper (TM), Thermal Infrared Multispectral Scanner (TIMS), and Airborne Imaging Spectrometer (AIS) data as part of a three-year research program to evaluate the utility of remote sensing measurements for analysis of sedimentary basins. The purpose of this research effort, which involves scientists from JPL, Hawaii Institute of Geophysics, and the University of Wyoming, is to construct stratigraphic columns, map variations in the lithology, geometry, and structure of sedimentary rocks in the Wind River/Bighorn Basin area, Wyoming, and to integrate remote sensing data with conventional geological and geophysical data to constrain models of basin formation and evolution.

In the Deadman Butte area of the Wind River Basin, it has been possible to make a photogeologic interpretation based on a color composite multipolarization SAR image and, with minimal field checking, assign stratigraphic formation names to the photogeologic units (Figure 16). In addition, comparison of the multipolarization SAR image brightness with the stratigraphic column generated by Lang (1984), using TM data and the column derived from measured sections in a nearby area of the Wind River Basin (Woodward, 1957), shows that, in some cases, more stratigraphic units can be differentiated in the remote sensing images.

One of the main goals in mapping in a sedimentary environment is to detect facies changes within geologic formations that may indicate changes in the depositional environment. Facies changes may result in changes in vegetation type and density, changes in mineralogy of the rocks, or changes in grain size that may result in a change in outcrop morphology. These are all changes that can potentially be detected in remotely sensed images.

The main effort in the analysis of the multipolarization SAR data has been to understand how the polarization signature relates to these variations in lithology. Once the polarization signature is understood, we can use this information in conjunction with the compositional information derived from the TM, TIMS, and AIS data to determine the extended spectral signatures of the units. These extended spectral signatures can then be stored in a library and used to characterize surficial units in remote areas.

Preliminary analysis shows that there is a high correlation of image brightness with vegetation density, which in turn has a high correlation with rock type. However, there does not appear to be any correlation between image brightness and soil moisture, probably because the soil samples were very dry (1-6% soil moisture). In addition, there is a polarization anomaly in the

Frontier siltstone between previously mapped units that cannot be explained by variations in soil moisture or vegetation cover. Thus, future field measurements will concentrate on dielectric constant and surface roughness measurements to explain this signature.

## REFERENCES


Lang, H. R., E. D. Paylor, and J. E. Conel, 1984. "Spectral Stratigraphy: A New Tool for Correlation and Facies Analysis, Permian-Upper Cretaceous, Casper Arch Area, Wyoming." Geol. Soc. of America Abs. with Programs, Annual meeting, Reno, Nevada, p. 568.

Woodward, T. C., 1957. "Geology of Deadman Butte Area, Natrona County, Wyoming," AAPG Bull. 41, p. 212-262.


Figure 16. Using this color composite SAR image and minimal field checking, stratigraphic formation names have been assigned via photogeologic interpretation. In some cases, it has been possible to separate more units in the SAR image than had been previously mapped.

# COMPOSITE SAR IMAGE PHOTOGEOLOGIC INTERPRETATION



## COMPOSITE SAR IMAGE


## INTERPRETATION


RED = VH GREEN = HH BLUE = VV

## EXPLANATION

| | FORMATION | MEMBER | ABBR |
|---|---|---|---|
| LATE CRETACEOUS | FRONTIER | (BASAL) | Kf |
| | | CLAYSPUR BENTONITE | Kfcb |
| EARLY CRETACEOUS | MOWRY | | Kmr |
| | MUDDY | | Kmd |
| | THERMOPOLIS | | Kt |
| | CLOVERLY | | KJc |
| | MORRISON | | KJm |
| JURASSIC | SUNDANCE | REDWATER SHALE | Js |
| | | LAK (?) | |
| | | HULLET SANDSTONE | |
| | | STOCKADE BEAVER | |
| | | CANYON SPRINGS | |
| TRIASSIC | CHUGWATER | POPO AGIE | Tcal |
| | | CROW MOUNTAIN | |
| | | ALCOVA | |
| | | RED PEAK | Tcrp |
| | DINWOODY | LITTLE MEDICINE | Td |
| | | UNNAMED | |
| PERMIAN | PHOSPHORIA | ERVAY | Pp |
| | | UNNAMED | |
| | | FORELLE | |
| | | GLENDO | |
| | | MINNEKAHTA | |
| | | OPECHE | |
| | | NOWOOD | |
| PENN | TENSLEEP | | Pt |
| | AMSDEN | | |

# MAPPING DIVERSE FOREST COVER WITH MULTIPOLARIZATION AIRBORNE RADAR

J. P. Ford and D. E. Wickland

Jet Propulsion Laboratory

and

R. R. Sharitz

Savannah River Ecology Laboratory

Imaging radar backscatter in continuously forested areas contains information about the forest canopy; it also contains data about topography, landforms, and terrain texture. For purposes of radar image interpretation and geologic mapping we are interested in identifying and separating forest canopy effects from geologic or geomorphic effects on radar images. The objective of this investigation is to evaluate forest canopy variables in multipolarization radar images under conditions where geologic and topographic variables are at a minimum. A subsidiary objective is to compare the discriminatory capabilities of the radar images with corresponding optical images of similar spatial resolution.

The Savannah River Plant (SRP), South Carolina, forms a suitable test site. Situated on the upper Atlantic coastal plain, the area contains a range of vegetation associations from swamp and bottomland hardwoods, through pine plantations, to upland scrub oak. It is managed by the U.S. Forest Service and subdivided into timber compartments. Detailed records of the age and condition of forest stands within the timber compartments are maintained by the Forest Service. Plant communities in the SRP have been subjected locally to a variety of stresses that result from nuclear materials production, operation of coal-fired power plants, and storage of radioactive wastes.

The forest is underlain by extensive, gently dipping clastic sedimentary rocks, mostly Tertiary in age. Slopes are mostly gentle, with a maximum relief from lowland swamp to upland sandhills of about 100 m (Langley and Marter, 1973).

The primary data for this investigation consist of NASA-JPL airborne synthetic-aperture radar (SAR) images. Ancillary supporting data include records of the U.S. Forest Service, field observations by the authors and by members of the Savannah River Ecology Laboratory, and aerial photography.

## AIRBORNE SAR IMAGES

The airborne SAR images were acquired at L-band (24.6 cm wavelength) simultaneously in four linear polarization states (HH, HV, VH, VV), with 10-m spatial resolution across a swath width of approximately 10 km. Each swath was acquired with two opposite directions of illumination. Figure 17 is a mosaic of optically correlated swaths with the same illumination direction.

Image areas that are representative of different forest types were selected for digital correlation and analysis. Since the data are automatically coregistered, the images in both the parallel-polarization states (HH and VV) and in one of the two cross-polarization states (HV or VH) were encoded as the red, green, and blue planes of color composite images. In this way differences in polarization signatures were evaluated and compared with detailed forest stand data provided by the U.S. Forest Service (Fig. 18).

Flooded forests appear very bright on images in all polarizations. Clearcuts and bodies of open water are very dark on images in all polarizations. Denser pine stands appear to have a strong cross-polarization response, and more open stands have a stronger response in the horizontal parallel polarization. Maps of forest stands in the timber compartments show that the most useful correlative forest data are stand basal area, forest age, site condition index, and forest management type. It appears that the multipolarization images discriminate variation in tree density, or difference in the amount of understory, but no evidence was found for discrimination between evergreen and deciduous forest types. Statistical correlation of the polarization signatures and the biophysical characteristics is in progress.

The deltas of Pen Branch and Four Mile Creek both receive thermal effluent from nuclear reactors on the SRP. The deltas have a unique polarization signature that seems to correlate with the location of heat-tolerant herbaceous plant communities on sandbars. Other stressed communities that are identifiable on the multipolarization images will be examined in detail.

## REFERENCE

Langley, T. M., and W. L. Marter. 1973. The Savannah River Plant Site, E. I. Dupont de Nemours and Co., Savannah River Laboratory, Aiken, South Carolina, DP-1323, 175 p.

Figure 17 (opposite page). This is a mosaic of optically correlated airborne SAR images, with outlines of locations chosen for digital processing and detailed analysis of multipolarization signatures. Areas are A, Pen Branch; B, Sand Hills; C, Ellenton Bay; D, Dunbarton Bays.

Figure 18 (following). This multipolarization false-color composite image shows polarization signatures of diverse forest cover at SRP in a 10 × 10 km area around Pen Branch. Swamp and flooded backwater areas appear very bright at all polarizations. Dense pine stands have strong cross-polarization response (blue). Adjacent more-open pine stands have stronger horizontal parallel polarization response (red). Clear cuts and bodies of open water provide weak responses and appear dark.

# Savannah River Plant, South Carolina

## March 1, 1984

POLARIZATION: HH

ORIGINAL PAGE
COLOR PHOTOGRAPH

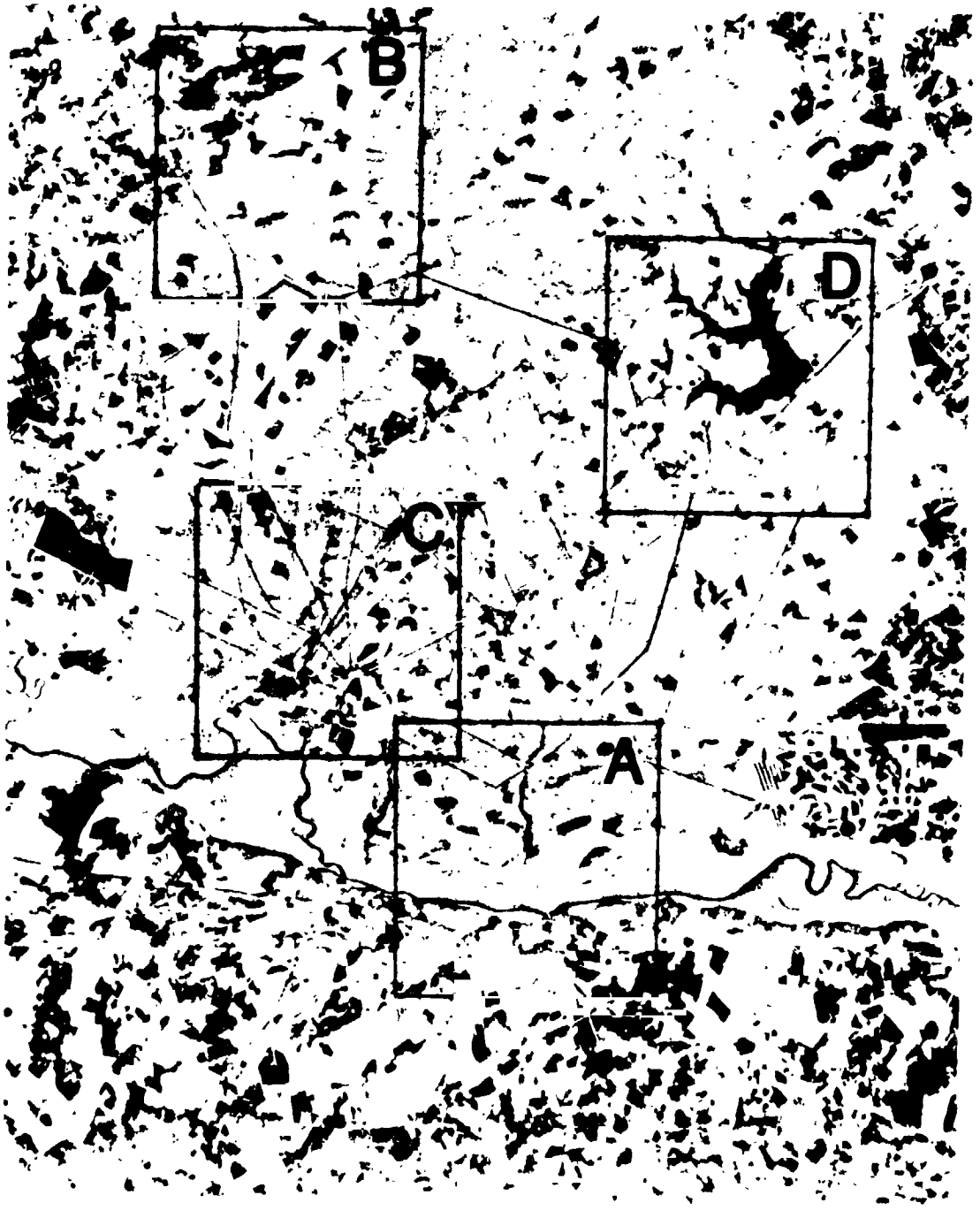


N

0 5 10km

RESOLUTION: ~10m

ILLUMINATION

ORIGINAL PAGE
COLOR PHOTOGRAPH

N86-10626

# POTENTIAL APPLICATIONS OF MULTIPOLARIZATION SAR FOR PINE PLANTATION BIOMASS ESTIMATION

S. T. Wu

NASA/National Space Technology Laboratories

This study was conducted as a part of the research tasks under the Radar Land Cover Analysis Program. The Radar Land Cover Analysis objective is, through utilization of multisensor data, to gain a basic understanding of the measurements and data characteristics in the visible-IR-microwave regions of the electromagnetic spectrum associated with specific surface features and cover types. Since the results of analysis of data acquired by Shuttle Imaging Radar (SIR-A) and Landsat Thematic Mapper (TM) over the study area were reported (NSTL/ERL Report No. 228, December 1984), this study focused on the analysis and evaluation of the L-band multipolarization airborne SAR data acquired over a southeastern pine forest scene. The data acquisition mission was flown on September 8 and 9, 1983. The HH, HV polarizations and the VV, VH polarizations were used on the first and the second day, respectively. Due to instrumentation difficulties, the digital recorder recorded only the second day's data. Because of this, only the VV and VH polarization data were used in this analysis. However, the HH and HV polarization images were available for visual comparison.

The study area, located in southwest Alabama, is part of the Gulf Coastal plain physiographic region referred to as the lower coastal plain. This particular area is representative of the longleaf-slash pine and oak-gum-cypress forest ecosystem found throughout the extreme southeastern United States. The longleaf-slash pine biome is typified by the presence of longleaf pine (Pinus palustris Mill) and slash pine (P. elliottii Engelm) Other southern yellow pine found throughout the area include loblolly pine (P. taeda L.), shortleaf pine (P. edunata Mill), and spruce pine (P. glabra Walt.). The majority of the upland portion of the study area is occupied by pine forest. Very little of the area supports agriculture, with most of the pine forest managed by forest industries. The composition of pine stands may range from uneven-aged mixed pine-hardwood to even-aged pine plantations. The upland drains contain various species of broadleaf evergreen shrubs, deciduous hardwood, and from 25% to 75% "turpentine" (old growth) pine. Fire is an important management tool in southern pine production; controlled burning is used to maintain the pine composition in the managed pine stands. In general, the study area contains a diversity of timber types, each maintained with various selections of forest management treatments. As a result, the study area is ideal for testing and evaluating SAR data characteristics in a forest regime.

To test the hypothesis that SAR data can be used to estimate forest biomass per unit area, the pine plantation plots were grouped according to the year of planting. Forest vegetation maps, completed by the International Paper Company, which manages the pine plantation sites, were used as a base to obtain the information regarding the year of planting, pine species, and area

coverage. Test plots were selected from the maps for planting ranging from 1958 to 1980. These plots were input as a polygon data file from which SAR data were extracted, including the number of pixels, the mean digital number (DN) and the coefficient of variation (COV) (Table 1). It appears that the mean DN, which is proportional to radar return signal strength, seems to correlate with the age of the pine plantation. It appears that the older the pine plantation, the higher its DN.

Alabama plantations contain similar silviculture treatments and biophysical parameters (localities, slopes, elevation, climate, soil types, etc.), but due to annual growth, an older pine plantation, in general, will contain higher above-ground biomass than that of a younger one. Based on this assumption, a "relative" index of green biomass (GBM) was assigned to each plot according to the year of planting. A simple linear regression using the index of GBM as an independent variable and the DN as a dependent variable for 27 pine plantation plots resulted in the following equations:

(1) SIR-A HH polarization

$$DN_{HH} = 77.2 + 3.69\ GBM \qquad R^2 = 0.74$$

(2) A/C SAR VV polarization

$$DN_{VV} = 84.9 + 2.98\ GBM \qquad R^2 = 0.79$$

(3) A/C SAR VH polarization

$$DN_{VH} = 71.1 + 3.35\ GBM \qquad R^2 = 0.80$$

It appears that SAR digital numbers correlate with the index of green biomass. In future studies, actual green biomass instead of the index of green biomass should be used to obtain a better biomass estimation algorithm. It is necessary to point out that the incidence angle variation of the aircraft SAR data varies from 5 degrees at the near range to 65 degrees at the far range. Because of this, the 27 pine plantation plots were selected from the far range area with incidence angle variation ranging from 45 to 60 degrees. It is assumed that the effect of the 15 degree incidence angle variation at far range is not sufficient to change the correlation results described previously.

TABLE 1. SAR DATA CHARACTERISTICS OF 27 PINE PLANTATION PLOTS

| PLOT ID | GBM INDEX | A/C SAR VV MEAN | A/C SAR VV COV | A/C SAR VH MEAN | A/C SAR VH COV | SR-A HH MEAN | SR-A HH COV | REMARKS |
|---|---|---|---|---|---|---|---|---|
| 801 | | 93.9 | 15.9 | 75.7 | 16.3 | 74.4 | 9.7 | |
| 802 | | 85.3 | 16.0 | 68.0 | 16.4 | 74.1 | 7.8 | |
| 8013 | | 89.0 | 16.0 | 62.5 | 16.5 | 72.2 | 8.6 | |
| 80 | 1 | 89.4 | | 68.7 | | 73.6 | | Av of 3 plots |
| 781 | | 109.3 | 16.8 | 97.2 | 16.9 | 85.2 | 10.6 | |
| 782 | | 98.9 | 20.4 | 92.8 | 18.5 | 81.3 | 11.2 | |
| 78 | 3 | 104.1 | | 95.0 | | 83.3 | | Av of 2 plots |
| 771 | 4 | 89.9 | 16.3 | 79.9 | 18.7 | 93.1 | 8.1 | |
| 751 | 6 | 102.7 | 16.9 | 90.1 | 17.4 | 100.9 | 11.2 | |
| 741 | | 88.3 | 17.8 | 87.2 | 19.4 | 94.1 | 11.5 | |
| 744 | | 92.0 | 13.1 | 72.6 | 22.6 | 86.3 | 9.8 | |
| 745 | | 109.5 | 15.8 | 90.6 | 18.9 | 103.5 | 11.9 | |
| 746 | | 104.9 | 18.3 | 89.3 | 20.7 | 105.5 | 9.4 | |
| 74 | 7 | 98.7 | | 84.9 | | 97.4 | | Av of 4 plots |
| 731 | | 108.8 | 17.6 | 100.0 | 17.3 | 114.7 | 8.9 | |
| 732 | | 115.6 | 15.2 | 107.7 | 17.3 | 118.7 | 8.4 | |
| 733 | | 108.3 | 17.4 | 106.8 | 18.7 | 117.0 | 5.7 | |
| 734 | | 113.8 | 17.3 | 104.6 | 16.9 | 130.5 | 7.5 | |
| 73 | 8 | 111.6 | | 104.8 | | 120.2 | | Av of 4 plots |
| 711 | 10 | 108.2 | 16.7 | 103.9 | 16.7 | 136.8 | 8.5 | |
| 701 | 11 | 112.1 | 17.2 | 107.9 | 18.5 | 116.8 | 7.1 | |
| 681 | 13 | 137.8 | 19.5 | 123.5 | 17.0 | 113.1 | 6.7 | |
| 671 | 14 | 121.7 | 17.0 | 106.6 | 17.7 | 130.4 | 10.0 | |
| 661 | | 138.3 | 17.9 | 132.4 | 19.7 | 126.3 | 7.4 | |
| 662 | | 140.4 | 16.7 | 129.8 | 15.6 | 115.9 | 6.0 | |
| 663 | | 116.4 | 12.8 | 112.1 | 16.0 | 127.1 | 7.5 | |
| 66 | 15 | 131.7 | | 124.8 | | 123.1 | | Av of 3 plots |
| 613 | | 86.4 | 17.8 | 64.3 | 20.8 | 122.1 | 8.5 | Clear-cut after |
| 581 | | 76.1 | 18.8 | 93.4 | 20.9 | 140.5 | 8.1 | SIR-A mission |
| 582 | | 133.6 | 16.5 | 195.9 | 15.5 | 150.9 | 6.5 | |
| 583 | | 127.6 | 18.4 | 169.0 | 20.0 | 139.9 | 9.9 | |
| 584 | | 135.1 | 18.2 | 205.8 | 13.5 | 149.7 | 9.9 | |

$DNVV = 84.9 + 2.98GBM$, $R^2 = 0.79$
$DNVH = 71.1 + 3.35GBM$, $R^2 = 0.80$
$DNHH = 77.2 + 3.69GBM$, $R^2 = 0.74$

N86-10627

# ON THE USE OF L-BAND MULTIPOLARIZATION AIRBORNE SAR FOR SURVEYS OF CROPS, VINEYARDS, AND ORCHARDS IN A CALIFORNIA IRRIGATED AGRICULTURAL REGION

Jack F. Paris

Jet Propulsion Laboratory

The airborne L-band synthetic aperture radar (SAR) collected multipolarization calibrated image data over an irrigated agricultural test site near Fresno, CA, on March 6, 1984. At this time, the region contained numerous fields of alfalfa having heights up to 40 cm, fields of barley and oats near heading, vineyards (Thompson Seedless and various wine grapes), and orchards (almonds, plums, walnuts, pecans, and peaches). Many fields were bare and furrowed for cotton planting. The aircraft flew three headings which enabled the SAR to look north, northeast, and east over sensor look angles from near the nadir to 55 degrees from the nadir. In the case of vineyards, severe effects were observed in the north-looking and east-looking data due to the presence of horizontal, long wire trellises that supported the grapevines. The effect of these was to increase greatly the SAR image brightness, especially for HH, when the azimuthal look direction was perpendicular to the azimuthal direction of the trellises. Furrowed fields, prepared for cotton planting, also exhibited a strong dependence on azimuthal look direction for similar reasons. No row direction effects were observed for the alfalfa, barley, oats, and orchards.

To reduce the row direction effects, the author concentrated on the northeast looking SAR data (Figure 19). In this mode, all rows were viewed at a 45 degree relative azimuthal angle. The conclusions of the study are as follows: (1) The effects of incidence angle on the measured backscattering coefficients could be removed by using a correction factor equal to the secant of the angle raised to the 1.4 power. (2) For this scene and time of year, the various polarization channels were highly correlated such that the use of more than one polarization added little to the ability of the radar to discriminate vegetation type or condition; the exception was barley which separated from vineyards only when a combination of like and cross polarization data were used. Polarization was very useful for corn identification in fall crops. (3) An excellent separation between herbaceous vegetation (alfalfa, barley, and oats) or bare fields and trees in orchards existed in brightness for all channels. (4) Within the alfalfa classes, the brightness was well correlated to alfalfa height or biomass, especially for the HH polarization combination. (5) Vineyards exhibited a narrow range of brightnesses with no systematic effects of type or number of stakes nor of number of wires in the trellises nor of the size of the vines. (6) Within the orchard classes, areal biomass [characterized by basal area] differences caused radar image brightness differences for small to medium trees but not for medium to large trees.

Figure 19. This image was a primary source for discrimination of crop type and biomass

# VEGETATION CANOPY DISCRIMINATION AND BIOMASS ASSESSMENT USING MULTIPOLARIZED AIRBORNE SAR

F. T. Ulaby and M. C. Dobson

University of Michigan

and

D. N. Held

Jet Propulsion Laboratory

Multipolarized airborne SAR data were acquired over a largely agricultural test site near Macomb, Illinois, in conjunction with the Shuttle Imaging Radar (SIR-B) experiment in October 1984. The NASA/JPL L-band SAR operating at 1.225 GHz made a series of daily overflights with azimuth view angles both parallel and orthogonal to those of SIR-B. The SAR data was digitally recorded in the quadpolarization configuration. An extensive set of ground measurements were obtained throughout the test site and include biophysical and soil measurements of approximately 400 agricultural fields.

Preliminary evaluation of some of the airborne SAR imagery indicates a great potential for crop discrimination and assessment of canopy condition. False color composites constructed from the combination of three linear polarizations (HH, VV, and HV) were found to be clearly superior to any single polarization for purposes of crop classification. In addition, an image constructed using the HH return to modulate intensity and the phase difference between HH and VV returns to modulate chroma indicates a clear capability for assessment of canopy height and/or biomass. In particular, corn fields heavily damaged by infestations of corn borer are readily distinguished from non-infested fields.

The SIR-B test site is characterized by relatively flat terrain with silt loam soils. The agricultural fields are typically 16 to 32 hectares (40 to 80 acres) in size and had been planted to approximately 45 percent corn, 45 percent soybeans, and 10 percent other crops (i.e., clover, alfalfa, sorghum, and pasture). Due to an unusually wet spring, planting was delayed and consequently, at the time of the SIR-B mission, only about 50 percent of the soybean acreage and 10 percent to 20 percent of the corn acreage had been harvested. In addition, the area had experienced widespread and occasionally severe infestations of European corn borer (Ostrinia Nubilalis). One effect of corn borer damage is to weaken the stalk and cause it to break and topple to the ground or remain hinged at the break point. The average height of corn stalks was 280 cm and 170 cm for unbroken and damaged stalks, respectively. Average vegetation characteristics are shown in Table 2.

During the SIR-B experiment approximately 400 fields were surveyed for crop inventory within a 200 $km^2$ area. Of these, about one half were sampled for more detailed measurements of crop biophysical parameters and soil moisture (on a daily basis). The airborne SAR imagery examined for this study contains about 40 percent of these fields.

TABLE 2. VEGETATION CHARACTERISTICS

| Crop | Part | Average Height (cm) | % Plant Moisture (wet basis) | Wet Biomass ($kg/m^2$) | % of Total Plant Water |
|---|---|---|---|---|---|
| Alfalfa | Whole | 10-20 | 80% | 1.9 | - |
| Clover | Whole | 10 | 75% | 1.2 to 5.0 | - |
| Soybeans | Whole | 90-100 | 15 to 20% | 1.5 | - |
| Cut Beans | Stubble & Litter | 15 | 10 to 20% | 0.5 to 1.0 | - |
| Corn | Whole | 280 undamaged | - | 5.0 | 100% |
| | | 170 borer damaged | | | |
| | Stalks | - | 75% | 2.4 | 78% |
| | Cobs | - | 15 to 30% | 2.0 | 19% |
| | Leaves | - | 10 to 20% | 0.5 | 3% |
| Cut Corn | Stubble & Litter | 30 | 40 to 50% | 1.2 to 2.5 | |

A false color composite of the multipolarized SAR data for part of the test site is shown in Figure 20. The additive colors red, green, and blue are driven by the magnitudes of the radar backscatter recorded for polarizations of HH, VV, and HV, respectively. In addition, a polarization phase-difference image was also generated for the overflight of the site on October 8, 1984. The resultant image, seen in Figure 21, is color coded by the phase-difference information (from $-\pi$ to $+\pi$) and the pixel intensity is proportional to the uncalibrated magnitude of the HH polarized return. The images are not corrected for STC or antenna gain variations across the swath. Field-by-field comparison of the phase-difference image to the crop survey observations yields the following general comments:

Figure 20. In this slant-range phase-difference image, there may be a correlation between the amount of yellow and magenta spotting in blue corn fields and the severity of corn-borer damage.

1. Soybeans, clover, alfalfa, pasture and bare soil (including corn and soybean stubble) always appear as various shades of magenta on the image. This color corresponds to a phase difference of $0^{o}$. The intensity is related to crop-type, soil roughness, and soil moisture as a function of incidence angle.

2. Standing corn fields, unharvested, always appear as blue to turquoise in color at incidence angles greater than about $25^{o}$ (from nadir). This color corresponds to a phase difference $\Delta\phi$ of about $180^{o}$.

3. The unharvested corn fields are generally not solid in color, but contain variable quantities of yellow and magenta spots. The yellow color corresponds to a phase difference $\Delta\phi = 90^{o}$ (yellow) and is correlated to the severity of corn borer damage (broken stalks). Table 3 shows that as the areal extent of damage by corn borers increases, the field exhibits an increasing spatial density of $0^{o}$ and $90^{o}$ phase difference.

Model calculations indicate that the color banding of corn fields, related to $\Delta\phi$, should vary across the image swath as a function of incidence angle. This expectation needs to be tested against the measured aircraft SAR data in a quantitative fashion before any definitive conclusions can be reached. On the other hand, model calculations indicate that the phase data contains useful scene information which may not be as readily extractable from magnitude data alone. As a consequence, the phase-difference approach warrants further investigation.

Figure 21. This three-color composite displays the relative magnitudes of the various polarization returns; the preceding image shows relative phase differences.

TABLE 3. MAG/PHASE CROP DISCRIMINATION

| Crop | Condition | No. of Fields | % of Total Fields | % of Crop Observed | | | | | |
|---|---|---|---|---|---|---|---|---|---|
| | | | | Magenta | | | Blue | | |
| | | | | Dark | Med | Bright | Solid | Yellow and Magenta Spots | |
| | | | | | | | | Few | Many |
| Corn | No damage | 6 | 14 | | | | 7 | 7 | |
| | Little damage | 5 | 11 | | | | | 11 | |
| | Some damage | 27 | 61 | | | | | 50 | 11 |
| | Much damage | 6 | 14 | | | | | 7 | 7 |
| | Total | 44 | 100 | | | | 7 | 75 | 18 |
| | Condition Not Known | 34 | 100 | | | | 3 | 94 | 3 |
| Corn Stubble | Cut | 10 | 100 | 50 | 30 | 20 | | | |
| Soybeans | Not harvested | 34 | 100 | 90 | 10 | | | | |
| Soybean Stubble | Cut | 36 | 100 | 72 | 14 | 14 | | | |
| Bare | Med rough | 3 | 75 | 50 | 25 | | | | |
| | Rough | 1 | 25 | | 25 | | | | |
| | Total | 4 | 100 | 50 | 50 | | | | |
| Clover, Alfalfa, and Pasture | | 12 | 100 | 45 | 47 | 8 | | | |
| Total Fields | | 174 | | | | | | | |

N86-10629

# MODELLING OF VEGETATION VOLUMES

Jakob J. van Zyl and Charles H. Papas

California Institute of Technology

and

Nader Engheta and Charles Elachi

Jet Propulsion Laboratory

The purpose of this discussion is to describe work that is being done to find theoretical models to describe radar backscatter from vegetation layers. The geometry of the problem is shown in Figure 22(a): A layer of thickness L containing a number of different scattering centers covers a ground surface.

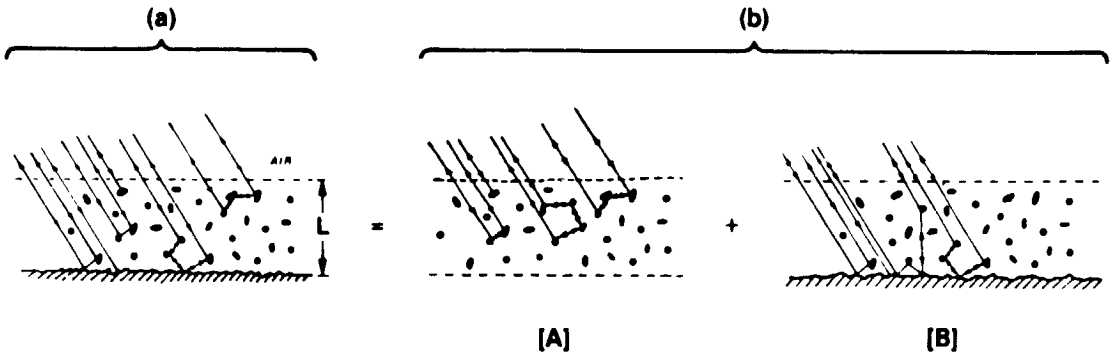


Figure 22. Scattering geometry.

The information that one would like to find through the application of the results of these models would include:

- The thickness of the layer.
- The absorption in the layer (i.e., density, moisture content, and biomass).
- The geometry of the scatterers (i.e., shape and orientation).
- How much of the received power is due to volume scattering only.
- A way to enhance the ratio of scattering that has some interaction with the ground surface.

The proposed ways to find this information are:

- Separate the scattering processes into volume scattering only and interaction between surface and volume scattering as in Figure 22(b). Once the scattering matrices [A] and [B] are known, the ratio of scattering due to one process to the other can be enhanced by using the optimum polarization for discrimination between [A] and [B].

- o The qualitative role of volume scattering can be found through the use of the optimum polarization of [A].
- o [A], and its response to different polarizations, will reveal some information about the geometry of the scatterers in the layer.
- o To find the rest of the information, a number of models to describe scattering from a selection of combinations of the basic types of scatterers must be developed.

The theoretical formulation of these models is done in terms of the bistatic scattering matrix of each of the types of scatterers present in the layer and their distribution (statistical or deterministic) in the layer. This formulation assumes that scatterers are small enough so that only dipole moments need to be considered and that the spacing of scatterers is such that shadowing of one scatterer by another may be neglected. The formulation allows more than one type of scatterer to be present in the same layer. The resulting effective scattering operator is expressed as an infinite sum, each term representing a particular order of scattering operator up to any order of accuracy by including more terms. At the same time this also gives direct information about the importance of multiple scattering.

Figure 23 (a)-(d) shows single scattering results for a layer consisting of 50% small dielectric spheres (e=6) of radius a=.15 wavelengths and 50% vertical dipoles (dipole moment p=.01) covering a ground surface (e=3) that scatters according to the Bragg relations. The results shown are for different layer thicknesses. The ground surface is assumed to have an inverse squared power spectrum. Also shown in parts (e) and (f) are single scattering results for layers consisting of spheres (e=6; a=.2 wavelengths) only and of vertical dipoles (p=.005) only. Both these layers are suspended in air--i.e. only volume scattering is considered. In all cases the scatterers are assumed to be uniformly and randomly distributed in the layer, and an average scatterer density of 64 scatterers per cubic meter is assumed. The wavelength used in these calculations is 23.5 cm. Figure 23 (a)-(d) clearly shows that the behavior of the backscatter coefficient is a strong function of the polarization basis as well as the layer thickness. Figure 23 (d)-(f) shows the strong dependence of the backscatter coefficient on the composition of the layer.

From the preliminary results of this work it appears that polarization may be a valuable tool in analyzing scattering results. Future work will be aimed at exploring the use of polarization in these situations in more detail. The importance of multiple scattering and its influence on the polarization characteristics of the layer will also be investigated in the near future.

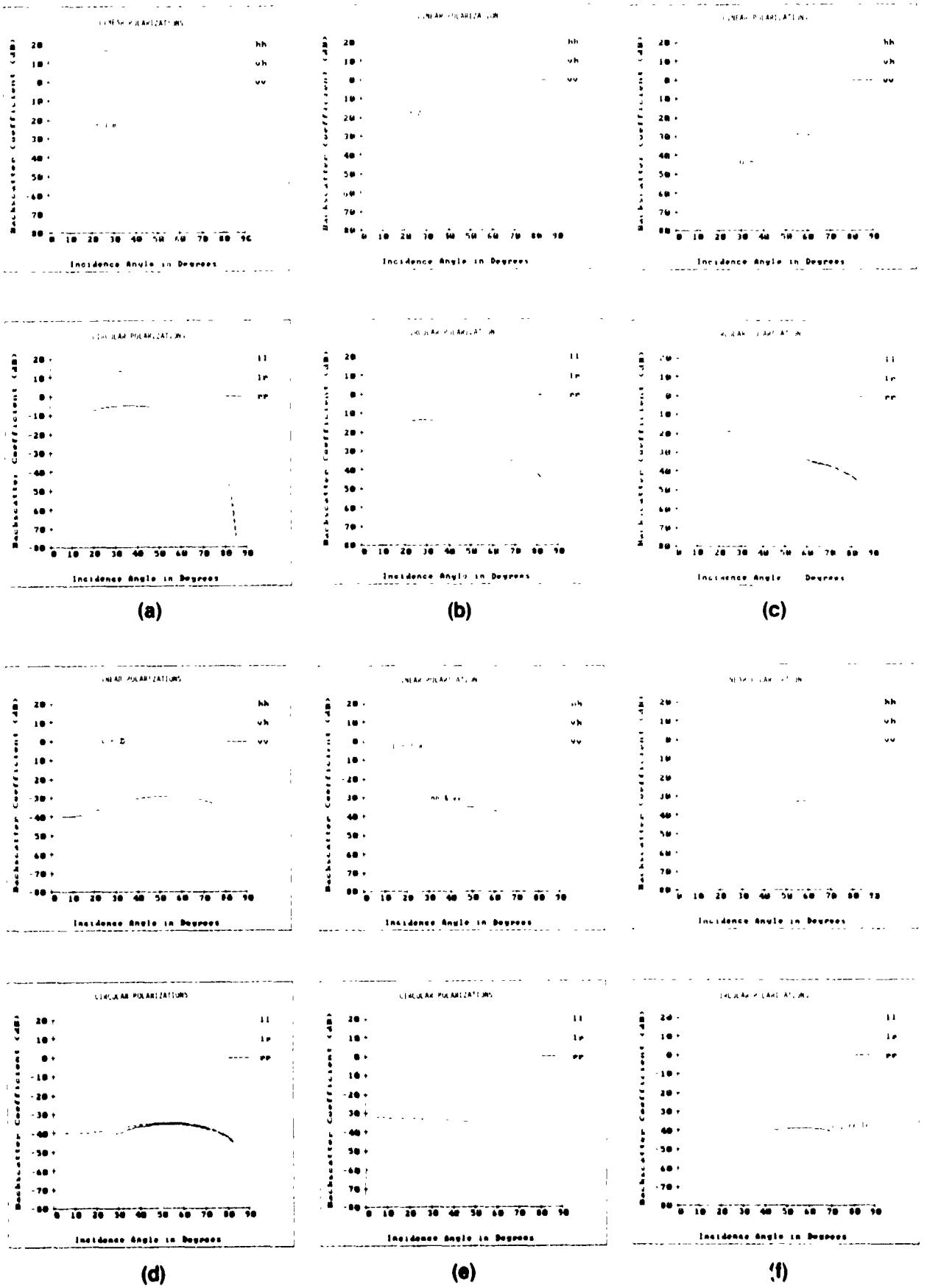


Figure 23. Single scattering results.

# APPENDIX A

# AIRCRAFT RADAR PERFORMANCE PARAMETERS

# AS OF FALL, 1984

SENSOR

| | |
|---|---|
| FREQUENCY | 1225 MHz |
| WAVELENGTH | 24.6 cm |
| PULSE LENGTH | 4.9 microsec |
| BANDWIDTH | 19.8 MHz |
| PRF AT 927 km/h (500 knots/h) | 750 Hz |
| PEAK POWER | 4 kW |

ANTENNA

| | |
|---|---|
| POLARIZATION | LINEAR HORIZONTAL AND VERTICAL |
| RANGE BEAMWIDTH | 70 degrees |
| AZIMUTH BEAMWIDTH | 8 degrees |
| POLARIZATION ISOLATION | ---------- |

DIGITAL RECORDING

| | |
|---|---|
| A/D SAMPLING RATE | 40 mega samples/sec |
| CHANNELS | 2 |
| WORD SIZE | 6 bits |
| BUFFER SIZE | 8192 words |
| TAPE RECORD RATE | $6.6 \times 10^6$ words/sec (40 megabits/sec) |
| RECORD SPEED | 305 cm/s (120 ips; 10 ft/s) |
| TAPE FOOTAGE | 2805 m (9200 feet) |

OPTICAL RECORDING

| | |
|---|---|
| SWEEP TIME | 55 microsecond |
| FILM WIDTH | 25 mm per channel |
| CHANNELS | 4 |
| START TIME | PROGRAMMABLE |
| DYNAMIC RANGE | 12 dB |

DIGITAL IMAGE

| | |
|---|---|
| SIZE | 1024 by 927 pixels (11.3 by 6.9 km slant range) |
| AZIMUTH PIXEL SPACE | 1[illegible] meters |
| AZIMUTH RESOLUTION | 13 meters |
| NUMBER OF LOOKS | 4 |
| SLANT RANGE PIXEL SPACE | 7.5 meters |
| SLANT RANGE RESOLUTION | 7.6 meters |
| INCIDENCE ANGLE COVERAGE | 0 to 75 degrees |

AIRCRAFT

| | |
|---|---|
| ALTITUDE RANGE | 1000 to 11,000 m (3000 to 36,000 ft) |
| NOMINAL ALTITUDE | 8839 m (29,000 ft) barometric |
| VELOCITY RANGE | 150 to 300 m/s |
| NOMINAL VELOCITY | 200 m/s (approximately 400 knots) |
| DRIFT ANGLE | ± 10 degrees |
| NOMINAL MAX. FLIGHT TIME | 6 hours |
| NOMINAL RANGE | 4828 km (3000 mi.) |
| AIRCRAFT ROLL ERROR | ± 0.1 degree |

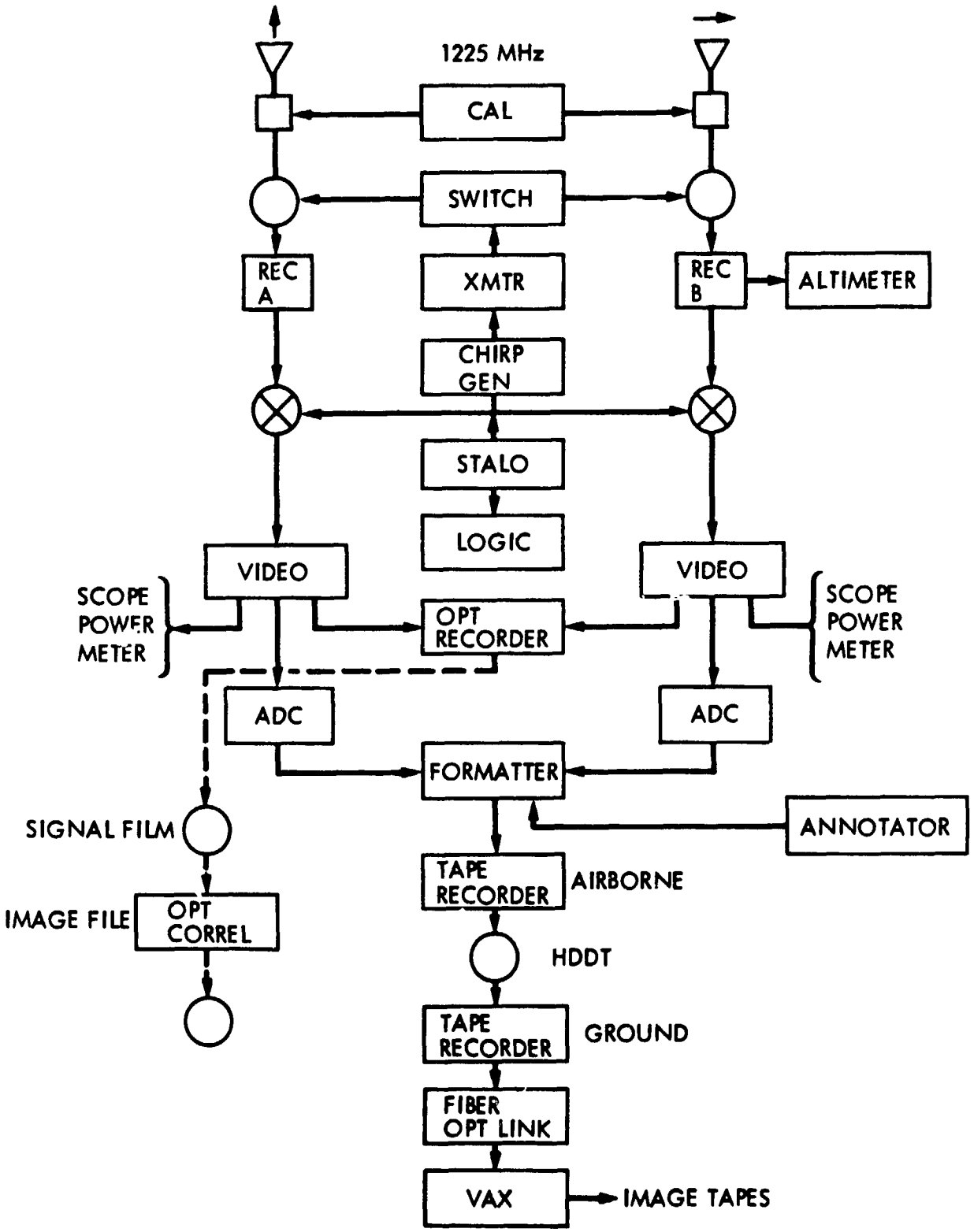


Figure A-1. Block diagram of JPL aircraft L-band SAR system from antenna to output imagery.

# APPENDIX B

## NASA/JPL AIRCRAFT RADAR WORKSHOP AGENDA

February 4-5, 1985
Jet Propulsion Laboratory
Building 167 Conference Room

February 4

8:30 - 12:30 Formal Presentations

| | |
|---|---|
| Introduction and Program Status | Dan Held, Walt Brown, Tommy Thompson/JPL |
| Absolute Calibration of Spring '84 SAR Data | Dan Held/JPL |
| Neogene Compressive Tectonism and Possible Thrust Faulting in Southwest Dominican Republic: Results from the 1982 SAR Mapping Mission | Tim Dixon/JPL |
| The Effect of Vegetation Type, Microrelief and Incidence Angle on Radar Backscatter (with Peggy O'Neill, Thomas Jackson, and Thomas Schmugge) | Manfred Owe/GSFC |
| Relative Age Dating of Volcanic and Alluvial Surfaces with Multipolarization Scatterometer and SAR Data (with Ron Blom) | Tom Farr/JPL |
| The Effects of Merging TM and A/C Radar on Wetland Classification | Jim Ormsby/GSFC |

12:30 - 1:30 Lunch

1:30 - 5:00 Discussions

| | |
|---|---|
| On the Measurement of Complete Scattering Matrices of Surfaces | Howard Zebker/JPL |
| Radar-Interferometric Determination of Topography | Dan Held, Howard Zebker/JPL |
| Strategies for Analyzing Mixed Pixels in Remotely Sensed Images | John Adams, Milton Smith/U. of Washington |

February 5

8:30 - 12:30 Formal Presentations

| | |
|---|---|
| Lithologic Mapping in a Sedimentary Environment using Multipolarization SAR Images (with Leslie Schenck) | Diane Evans/JPL |
| Mapping Diverse Forest Cover With Multipolarization Airborne Radar (with D. E. Wickland and R. R. Sharitz) | John Ford/JPL |
| Potential Applications of Multipolarization SAR for Pine Plantation Biomass Estimation | S. T. Wu/NSTL |
| Use of L-Band Multipolarization SAR for Surveying Crops, Vineyards, and Orchards in a California Irrigated Agricultural Region | Jack Paris/JPL |
| Vegetation Canopy Discrimination and Biomass Assessment Using Multipolarized Airborne SAR (with F. T. Ulaby and D. N. Held) | Craig Dobson/U. of Michigan |
| Forest Signatures at X- and L-Band: Results from the SAR580 and DFVLR Scatterometer | Alois Sieber/U. of Stuttgart |

12:30 - 1:30 Lunch

1:30 - 5:00 Discussions

| | |
|---|---|
| Modelling of Vegetation Volumes | Nader Engheta, Jakob Van Zyl/Caltech |
| Field Measurements of Surface Roughness and Soil Moisture | Tom Farr, Ron Blom/JPL |
| Summary and Recommendations | All |

# APPENDIX C

## NASA/JPL AIRCRAFT SAR WORKSHOP ATTENDEES

| | |
|---|---|
| John Adams | University of Washington |
| Ron Blom | Jet Propulsion Laboratory |
| Marcus Borengasser | University of Nevada, Reno |
| Walt Brown | Jet Propulsion Laboratory |
| Frank Carsey | Jet Propulsion Laboratory |
| Keith Carver | University of Massachusetts |
| Pamela Clark | Jet Propulsion Laboratory |
| Josef Cihlar | Canada Centre for Remote Sensing |
| Tim Dixon | Jet Propulsion Laboratory |
| Craig Dobson | University of Michigan |
| Neva Donovan | Jet Propulsion Laboratory |
| Stephen Durden | Stanford University |
| Charles Elachi | Jet Propulsion Laboratory |
| Ted Engman | USDA ARS Hydrology Laboratory |
| Diane Evars | Jet Propulsion Laboratory |
| Thomas Farr | Jet Propulsion Laboratory |
| John Ford | Jet Propulsion Laboratory |
| Lisa Gaddis | University of Hawaii |
| Richard Goldstein | Jet Propulsion Laboratory |
| Hugh Gwyn | Universite de Sherbrooke |
| Philipp Hartl | University of Stuttgart |
| Daniel Held | Jet Propulsion Laboratory |
| Roger Hoffer | Purdue University |
| Tak Hoshizaki | Jet Propulsion Laboratory |
| Verne Kaupp | University of Arkansas |
| Catherine Kitcho | NASA Headquarters |
| Richard Kozak | U.S. Geological Survey |
| Leo Krul | Delft University of Technology |
| Thuy LeToan | Universite Paul Sabatier de Toulouse |
| Edward Link | USAE Waterways Experiment Station |
| Warren Lushbaugh | Jet Propulsion Laboratory |
| Chuck Luther | Office of Naval Research |
| Mike McDonnell | DSIR, New Zealand |
| Paul Merifield | Lamar-Merifield, Geologists Inc. |
| Richard Monson | NASA Headquarters |
| Peter Mouginis-Mark | University of Hawaii |
| Wolfgang Noack | DFVLR |
| Wes Norris | Earth Technology Corporation |
| Herwig Oettl | DFVLR |
| Jim Ormsby | Goddard Space Flight Center |
| Steve Ostro | Jet Propulsion Laboratory |
| Manfred Owe | Goddard Space Flight Center |
| Mimi Paller | Jet Propulsion Laboratory |
| Jack Paris | Jet Propulsion Laboratory |
| Clair Parker | NAVELEX |
| Jay Parrish | Jet Propulsion Laboratory |
| Earl Peterson | NASA Ames |
| David Pitts | Johnson Space Center |
| John Reller | NASA/Ames |
| M. Ricottilli | CNR/PSN, Italy |
| Martin Ruzek | Jet Propulsion Laboratory |
| Floyd Sabins | Chevron Oil Field Research |
| Leslie Schenck | Jet Propulsion Laboratory |

| | |
|---|---|
| Milton Smith | University of Washington |
| Alois Sieber | University of Stuttgart |
| Ray Suguira | Earth Technology Corporation |
| James Taranik | University of Nevada-Reno |
| Sid Theis | Texas Instruments |
| Robert Thomas | NASA Headquarters |
| Tommy Thompson | Jet Propulsion Laboratory |
| Fawwaz Ulaby | University of Michigan |
| Jim Vogelman | Jet Propulsion Laboratory |
| Jim Wang | Goddard Space Flight Center |
| Ron Wasowski | Notre Dame |
| Walt Westman | NASA/Ames |
| Diane Wickland | Jet Propulsion Laboratory |
| S. T. Wu | NSTL |
| William Yang | Jet Propulsion Laboratory |
| Howard Zebker | Jet Propulsion Laboratory |